Author Manuscript

Author Manuscript

Author Manuscript

Author Manuscript

HHS Public Access

Author manuscript

J Theor Biol. Author manuscript; available in PMC 2016 May 21.

Published in final edited form as:

J Theor Biol. 2015 May 21; 373: 26–39. doi:10.1016/j.jtbi.2015.03.004.

Quantification and simulation of layer-specific mitral valve interstitial cells deformation under physiological loading

Chung-Hao Lee[a], **Christopher A. Carruthers**[b], **Salma Ayoub**[a], **Robert C. Gorman**[c], **Joseph H. Gorman III**[c], and **Michael S. Sacks**[a]

[a]Center for Cardiovascular Simulation, Institute for Computational Engineering and Sciences (ICES), Department of Biomedical Engineering, The University of Texas at Austin, 201 East 24th Street, POB 5.236, 1 University Station C0200, Austin, TX 78712, USA

[b]Cardiac Rhythm Disease Management (CRDM) Clinical Specialist, Medtronic, Minneapolis, MN 55432, USA

[c]Gorman Cardiovascular Research Group, University of Pennsylvania, 3400 Civic Center Blvd, Philadelphia, PA 19104, USA

Abstract

Within each of the four layers of mitral valve (MV) leaflet tissues there resides a heterogeneous population of interstitial cells that maintain the structural integrity of the MV tissue via protein biosynthesis and enzymatic degradation. There is increasing evidence that tissue stress-induced MV interstitial cell (MVIC) deformations can have deleterious effects on their biosynthetic states that are potentially related to the reduction of tissue-level maintenance and to subsequent organ-level failure. To better understand the interrelationships between tissue-level loading and cellular responses, we developed the following integrated experimental-computational approach. Since in-vivo cellular deformations are not directly measurable, we quantified the in-situ layer-specific MVIC deformations for each of the four layers under a controlled biaxial tension loading device coupled to multi-photon microscopy. Next, we explored the interrelationship between the MVIC stiffness and deformation to layer-specific tissue mechanical and structural properties using a macro-micro finite element computational model. Experimental results indicated that the MVICs in the fibrosa and ventricularis layers deformed significantly more than those in the atrialis and spongiosa layers, reaching a nucleus aspect ratio of 3.3 under an estimated maximum physiological tension of 150 N/m. The simulated MVIC moduli for the four layers were found to be all within a narrow range of 4.71–5.35 kPa, suggesting that MVIC deformation is primarily

© 2015 Published by Elsevier Ltd.

For correspondence. Michael S. Sacks, Ph.D., W. A. 'Tex' Moncrief, Jr. Simulation-Based Engineering Science Chair I, Director, Center for Cardiovascular Simulation, Institute for Computational Engineering and Sciences, Professor of Biomedical Engineering, The University of Texas at Austin, 201 East 24th Street, POB 5.236, 1 University Station C0200, Austin, TX 78712, USA, msacks@ices.utexas.edu, Tel: +1(512) 232-7773.

Publisher's Disclaimer: This is a PDF file of an unedited manuscript that has been accepted for publication. As a service to our customers we are providing this early version of the manuscript. The manuscript will undergo copyediting, typesetting, and review of the resulting proof before it is published in its final citable form. Please note that during the production process errors may be discovered which could affect the content, and all legal disclaimers that apply to the journal pertain.

Conflict of Interests

None of the authors have a conflict of interests with the present work.

Author Manuscript Author Manuscript Author Manuscript Author Manuscript

controlled by each tissue layer's respective structure and mechanical behavior rather than the intrinsic MVIC stiffness. This novel result further suggests that while the MVICs may be phenotypically and biomechanically similar throughout the leaflet, they experience layer-specific mechanical stimulatory inputs due to distinct extracellular matrix architecture and mechanical behaviors of the four MV leaflet tissue layers. This also suggests that MVICs may behave in a layer-specific manner in response to mechanical stimuli in both normal and surgically modified MVs.

Keywords

Finite element simulations; simplified structural constitutive model; MVIC microenvironment; MPM imaging analysis; multi-level macro-micro modeling

1. Introduction

Once largely considered as simple, passive fluidic functional components of the heart, heart valves are now deemed dynamic structures that actively remodel and have their own vasculature and innervation D'Amore et al., 2009; Sacks and Yoganathan, 2008). Mitral valve (MV) mechanical loading results from the combination of blood flow-induced fluid shear stresses, changes in annular and papillary dimensions, and cyclic pressure: all integrating to produce net tissue stresses. Within the four layers of the MV leaflet tissue, there resides a heterogeneous population of interstitial cells (Filip et al., 1986; Messier et al., 1994; Mulholland and Gotlieb, 1996; Taylor et al., 2003). Among all valve interstitial cells (VICs), mitral valve interstitial cells (MVICs) have characteristics of both fibroblasts and smooth muscle cells. Studies of VICs in both human and porcine valve tissues have revealed that the cells are not localized to any particular region or layer of the leaflet, but are present throughout the valve leaflet tissues (Bairati and DeBiasi, 1981; Merryman et al., 2006b).

Interest in VICs has grown in recent years as they are believed to be critically important in valve tissue homeostasis and pathophysiology. Primarily, VICs serve to maintain the structural integrity of the leaflet tissue via protein synthesis and enzymatic degradation. Their phenotype, which ranges from fibroblast-like to myofibroblast-like, is plastic and reversible. VICs in normal healthy valves are quiescent, whereas they become activated and contractile in pathological valves (Rabkin-Aikawa et al., 2004; Rabkin et al., 2002). While their dualistic nature is not fully understood, the multi-functionality of VICs may involve cell-to-cell communication, tissue remodeling, wound healing, and contraction (Mulholland and Gotlieb, 1996). When the phenotype of the resident VICs is myofibroblast-like, the cells are actively remodeling the extracellular matrix (ECM), indicating that VIC phenotypic state at a given time is related to the current remodeling demands of the tissue (Rabkin et al., 2002). Recent work by Grande-Allen demonstrated the interrelationship between substrate stiffness, VIC phenotype and synthetic properties (Grande-Allen and Liao, 2011; Stephens et al., 2010a; Stephens et al., 2011). Simmons used micropipette aspiration techniques to quantify the elastic properties of VICs. Their results indicated that the VIC elastic modulus increases with pathological differentiation (Wyss et al., 2012), and that VIC phenotypic

Author Manuscript Author Manuscript Author Manuscript Author Manuscript

plasticity and mechanical adaptability are regulated both biomechanically and biochemically, which, in turn, affect the progression of diseases and pathologies.

Our group has demonstrated that VICs from the aortic and mitral valves are significantly stiffer than those from the pulmonary and tricuspid valves (Merryman et al., 2007; Merryman et al., 2006c). By quantifying collagen biosynthesis and cytoskeletal composition using alpha-smooth muscle actin (α-SMA) and the molecular chaperone heat-shock protein 47 (HSP47) as bio-indicators, we found that the mitral and the aortic VICs contain significantly more α-SMA and HSP47 (Merryman et al., 2006a). Moreover, we found that the aortic VICs have a greater ability to contract free-floating collagen gels compared to the pulmonary VICs under identical experimental conditions (Merryman et al., 2007), indicating a greater ability to remodel collagenous soft tissues. This can be linked to the regulatory function of the endothelium on the mechanical properties of the aortic valve leaflets (El-Hamamsy et al., 2009). These studies revealed the unique properties of VICs to form cellular networks within collagen gels and spontaneously interact with the extracellular matrix to induce contractile forces. MVICs seeded in three-dimensional collagen gels could generate 50% of the total force significantly faster than the VICs of the aortic and tricuspid valves, suggesting that the distinct functional properties of VICs reflect the mechanical function of the heart valves (Smith et al., 2007).

In biomechanics, the presence of normal tissue stresses has long been considered to be closely related to tissue homeostasis (Chuong and Fung, 1986; Fung, 1991; Lanir, 2009; Ogden, 2003; Taber and Humphrey, 2001). Moreover, it has been shown that pathophysiological alterations in mechanical loading can lead to stress changes and subsequent tissue adaptation (Fung and Liu, 1991; Liu and Fung, 1989). In the MV, numerous pathological factors, such as tachycardia-induced cardiomyopathy (Stephens et al., 2009) and mitral regurgitation (Stephens et al., 2008), have been shown to affect MV tissue structure and extra-cellular matrix composition. Collectively, disease- and repair-induced alternations in MV geometry result in altered tissue stresses—these changes in tissue-level stresses and deformations could subsequently lead to tissue remodeling that would ultimately affect the long-term durability of MV surgical repair.

Advances in MV computational modeling and simulation research have been significantly made in the past two decades, including development of constitutive models for the MV tissues (May-Newman and Yin, 1998; Prot and Skallerud, 2009; Prot et al., 2007; Skallerud et al., 2011; Weinberg and Kaazempur Mofrad, 2007), image-based patient-specific computational modeling (Mansi et al., 2012; Stevanella et al., 2011; Votta et al., 2008; Wang and Sun, 2013), fluid-structure interaction modeling (Einstein et al., 2004; Kunzelman et al., 2007), inverse approaches for assessing the in-vivo biomechanical properties of the MV (Lee et al., 2014; Rausch et al., 2012), and coupled left ventricle-mitral valve modeling for investigating ischemic mitral regurgitation (Wenk et al., 2010). These efforts represent important steps towards the development of physiologically realistic models of functioning heart valves.

Yet, no existing models make the connection between organ- and tissue-scale simulations to cellular mechanotransduction and mechanobiological responses. Moreover, there is still a

Author Manuscript Author Manuscript Author Manuscript Author Manuscript

lack of quantitative data in the heart valve literature relating the regional tissue stress and homeostasis to the underlying cellular function. In particular, there is growing evidence that cyclic tissue strains can profoundly influence the biosynthetic responses of VICs, both *in vitro* (Balachandran et al., 2009b; Balachandran et al., 2006b; Carruthers et al., 2012b; Gupta et al., 2007; Gupta et al., 2009; Konduri et al., 2005) and *in vivo* (Quick et al., 1997; Stephens et al., 2009). Ideal phenomenological models should be able to simulate VIC behavior in response to mechanical inputs such as tissue-level and cellular strains and the induced cellular biosynthetic responses. Such a model would enable predictions of the phenotypic and biosynthetic responses of VICs due to altered valvular tissue stresses in various heart valve repair scenarios. Clearly, a necessary first step is the ability to predict layer-specific MVIC deformations from the macroscopic tissue deformations as presented in this work.

As in-vivo MVIC deformations cannot be measured directly with existing experimental techniques, we developed an integrated computational, in-situ experimental approach to explore the interrelationship between tissue stress, MVIC deformation and mechanical properties in the MV anterior leaflet (MVAL) tissue. First, we utilized a newly-developed in-vitro assessment technique to quantify the in-situ layer-specific MVIC deformations within each of the four layers of the MVAL tissues under controlled biaxial stretch over a range of physiological tension loading. This method allows us to acquire sufficient information to construct layer-specific computational models of the MV leaflet. Next, we incorporated available histological and microstructural information of the MVAL tissues into a macro-micro finite element (FE) computational framework for modeling both MVAL tissues and MVIC microenvironment. This integrated approach enabled the quantification of layer-specific MVIC deformations in the MVAL tissue under controlled biaxial tension loading, the estimation of the MVIC modulus, and the investigation of the interrelationship between MVIC stiffness and deformation to layer-specific mechanical and microstructural properties.

2. Methods

2.1 Valve tissue preparation and real-time deformation measurement

We begin by presenting the experimental methods to quantitatively characterize layer-dependent MVIC deformations under controlled physiological loading. First, fresh ovine hearts from 40 kg sheep were acquired from a local USDA approved abattoir. MV leaflets were dissected and the surrounding myocardium was carefully trimmed from the leaflets (Fig. 1-a). Tissue samples of 10 mm×10 mm were then taken from the center region of the MVAL, below the annulus and above the first chordae tendineae attachment site (Fig. 1-a, Fig. 2-a). The samples were loaded into a miniature biaxial testing system, in which the specimen's circumferential and radial directions were aligned with the device axes. Four graphite fiducial markers were placed in the center of each tissue sample and their positions were tracked optically in real time. The real-time tissue-level deformation gradient tensor **F** was computed by using standard surface strain calculation techniques (Sacks et al., 2006) based on the measured marker displacements using a single four-node bilinear finite element. The MV leaflets were loaded to 5, 10, 20, 50, 100, and 150 N/m, and $\overline{\lambda}_C$, $\overline{\lambda}_R$, and

Author Manuscript Author Manuscript Author Manuscript Author Manuscript

$\overline{\lambda}_T = 1/\overline{\lambda}_C \overline{\lambda}_R$, the tissue-level stretches in the circumferential, radial and transmural directions, respectively, were determined from **F** under the assumption of an incompressible material (Sacks, 2000).

2.2 Valve tissue fixation and imaging

Three tissue specimens (n=3) from the MVAL center region were measured at the unloaded state (0 N/m tension) and at each tension level, resulting in a total of 21 samples. Each sample was fixed in 2% aqueous paraformaldehyde (PFA) solution for 2 hours in the loaded configuration, and then split into two sections for the following analyses (Fig. 2-b). The first 7 μm section was stained with Movat's Pentachrome to distinguish the histologic four layers of the MV leaflet: atrialis, spongiosa, fibrosa, and ventricularis layers (Kunzelman et al., 1993; Sacks and Yoganathan, 2008), and to quantitatively measure the thickness changes and the microstructural compositions among different layers under biaxial tension loading. The second 30 μm section was paraffin-embedded and cryosectioned along the circumferential-transmural surface. The sample slides were then deparaffinized, permeabilized with Triton-X for 20 minutes, and stained with Sytox Green (Invitrogen Corp., CA, USA) at a 1:250 concentration for another 30 minutes. After being gelvatol-mounted and cover-slipped, each sample slide was taken for imaging under the multi-photon microscopy (MPM) system (Watkins, 2001) at an excitation wavelength of 830 nm with an incremental *z*-step of 1 μm. Here, the MPM was used to image the MVIC Cytox green nuclei via two-photon excited fluorescence (TPEF) with a TPEF-filter set up at 525±50 nm.

2.3 In-situ determination of MVIC nuclear orientation and deformation

MVIC nuclear orientation and deformation for each tissue layer and tension level were measured and analyzed as follows. The TPEF-MPM image stacks were first imported into Imaris software (Bitplane AG, Zurich, Switzerland) for 3D nuclear deformation visualization and quantitative analysis (Fig. 3-a). Individual surface was then fitted to each nuclear point cloud (Fig. 3-b), and erroneous detections were eliminated using an automated maximum voxel threshold and a minimum voxel threshold of 250 (Fig. 3-c). The eigenvectors associated with each 3D nuclear surface were determined based on an assumed MVIC ellipsoidal geometry (Fig. 4) using an in-house MATLAB program (The Mathworks Inc., Natick, MA, USA), and the corresponding major and minor axes of each MVIC ellipsoid were converted into the nuclear aspect ratio ($NAR=L_a/L_c$). Note that we utilized the NAR as a dimensionless indicator of MVIC deformation (Sacks et al., 2009). In addition, the eigenvectors for each cell were converted into the spherical coordinates to define the 3D orientation of each MVIC with orientation angles θ and φ. Moreover, the four layers of the MV tissue were identified from a maximum intensity *z*-projection of collagen networks on the MPM images, and the quantitative data of each MVIC nucleus was automatically associated with its respective layer (Fig. 3-d). Note that for each specimen, the nuclear aspect ratio and orientation angles of MVICs associated with each layer were determined and averaged over all the MVICs residing in each of the four different layers, and the mean (*n= 3 samples*) was then calculated and reported.

Author Manuscript Author Manuscript Author Manuscript Author Manuscript

2.4 Morphological analysis of layer-specific compositions and microstructures of the MVAL tissues

Layer-specific mass fractions of matrix and fibers (ω_m^ξ, ω_c^ξ, and ω_e^ξ) were determined by quantitatively assessing the Movat-stained and circumferentially-oriented MVAL sections using ImageJ (National Institute of Health, Bethesda, MD) in accordance with the methods previously described (Flanagan et al., 2006). Here, we adopted the subscripts m, c, e to denote matrix, collagen fiber and elastin fiber components, respectively, and the superscript ξ to denote the layer identifier, which refers to ξ=1-atrialis, 2-spongiosa, 3-fibrosa, and 4-ventricularis layers of the MVAL. The color deconvolution method (Ruifrok and Johnston, 2001) was adopted to separate the red/green/blue (RGB) image into collagen (yellow), elastin (black), and ground substance (blue) components. Background corrections were further applied by subtracting the integrated optical density (IOD), which is the sum of pixel values, from the white pixel intensity. For all three components, each layer was represented as a region of interest (ROI) and layer-specific mass fractions were calculated by $\omega_i^\xi = \mathrm{IOD}_i^\xi / (\mathrm{IOD}_m^\xi + \mathrm{IOD}_c^\xi + \mathrm{IOD}_e^\xi)$, i=m,c,e. In order to compensate for the layer-specific thicknesses, the above quantified layer-specific mass fractions were used to determine the volume fractions of matrix and collagen and elastin fibers: $\phi_m^\xi = \omega_m^\xi \times t^\xi / t_{leaflet}$, $\phi_c^\xi = \omega_c^\xi \times t^\xi / t_{leaflet}$ and $\phi_e^\xi = \omega_e^\xi \times t^\xi / t_{leaflet}$ as will be employed in the finite element modeling introduced in the subsequent sections, where t^ξ is the thickness of each layer and $t_{leaflet}$ is the total thickness of the MVAL tissue (Table 1).

Next, we employed the measured fiber splay structural data for each of the four layers using second harmonic generation (SHG) methods (Fata et al., 2013) and reported in (Carruthers et al., 2012b) to define the layer-specific material axial direction μ^ξ and the fiber splay standard deviation σ^ξ (Table 1). It should be noted that in our studies of MV fiber structure in (Carruthers et al., 2012b) the collagen and elastin fibers always coincided and had very similar orientation distributions, so we combined their collective effects into a single homogenized or effective fiber response. In addition, to be consistent with the experimental data, we utilized a Gaussian distribution function for representing the fiber angular orientation distribution of the measured fiber splay. The fiber splay was directly derived from the measured orientation index (OI) used in (Carruthers et al., 2012b) to denote the strength of fiber splay alignment. In that study, the OI was defined as the angular width in which 50% of the total number of fibers occurs. The fiber splay standard deviation σ^ξ associated with each of the four layers can be derived directly from the OI value using $\mathrm{erf}\left(\frac{\mathrm{OI}^\xi}{2\sqrt{2}\sigma^\xi}\right) - \frac{1}{2}\mathrm{erf}\left(\frac{180^\circ}{2\sqrt{2}\sigma^\xi}\right) = 0$ (Sacks et al., 1997).

2.5 Finite element model development

Next, we developed a multi-level computational framework at both macroscopic and microscopic scales to investigate the interrelationship between layer-specific mechanical behaviors and the measured MVIC deformations obtained in Section 2.3, which incorporated tissue-level deformations from the planar equi-biaxial tension loading of the MVAL tissue (Fig. 5-a) with the modeling of the MVIC microenvironment (Fig. 5-b)

Author Manuscript Author Manuscript Author Manuscript Author Manuscript

considering the layer respective microstructure and composition (Fig. 1-b). The details of the proposed computational modeling were described in the subsequent subsections.

2.5.1 FE modeling of the MVAL tissue under planar equi-biaxial tension loading—For FE modeling of the MVAL tissue under planar equi-biaxial tension loading, a specimen of the central region (10 mm × 10 mm) of the MVAL tissue was discretized into 400 (20×20) four-node membrane (M3D4) elements with a thickness of 0.422 mm, and uniform tractions were gradually applied on the four edges of the MVAL tissue from 0 to 150 N/m in order to simulate the experimental loading protocol. Adequate clamped boundary conditions were prescribed to avoid rigid-body motions in the FE numerical simulation. The mechanical behavior of the MVAL tissue was simulated by the following incompressible simplified structural model with an exponential form of the effective fiber ensemble stress, developed in our recent study (Fan and Sacks, 2014). This constitutive model was implemented in a user material subroutine in commercial finite element software ABAQUS 6.13 (SIMULIA, Dassault Systemes, Providence, RI, USA)

$$\mathbf{S}_{\text{leaflet}}=\sum_{\xi=1}^{4}\left\{\phi_{\text{m}}^{\xi}\mu_{\text{m}}\left(\mathbf{I}-\text{C}_{33}\mathbf{C}^{-1}\right)+\int_{-\pi/2}^{\pi/2}\Gamma^{\xi}(\theta)\text{S}_{\text{ens}}^{\xi}\left[\text{E}_{\text{ens}}(\theta),\text{c}_0,\text{c}_1\right]\mathbf{N}(\theta)\otimes\mathbf{N}(\theta)\text{d}\theta\right\}, \quad (1)$$

Where

$$\text{S}_{\text{ens}}^{\xi}\left[\text{E}_{\text{ens}}(\theta),\text{c}_0,\text{c}_1\right]=\phi_{\text{f}}^{\xi}\text{c}_0\left\{\exp\left[\text{c}_1\text{E}_{\text{ens}}(\theta)\right]-1\right\}. \quad (2)$$

Here, $\mathbf{S}_{\text{leaflet}}$ is the total tissue second Piola-Kirchhoff stress tensor, c_0, c_1, and μ_m are material constants (Table 2). Physically, μ_m represents the non-fibrous tissue components or "matrix" effective shear modulus. $\Gamma^{\xi}(\theta)$ and $\text{S}_{\text{ens}}^{\xi}$ are the fiber angular orientation distribution function and the effective fiber ensemble stress, respectively, associated with each layer ξ. $\text{E}_{\text{ens}}(\theta)=\mathbf{N}^{\text{T}}(\theta)\mathbf{E}\mathbf{N}(\theta)$ is the effective fiber ensemble strain, $\mathbf{N}(\theta)=[\cos(\theta),\sin(\theta)]^{\text{T}}$ is the unit vector defining the common preferred fiber direction of the fiber ensemble at the reference configuration, $\mathbf{E}=(\mathbf{C}-\mathbf{I})/2$ is the Green-Lagrange strain tensor, $\mathbf{C}=\mathbf{F}^{\text{T}}\mathbf{F}$ is the right Cauchy-Green deformation tensor, $\mathbf{F}$ is the deformation gradient, $\mathbf{I}$ is the second-rank identity tensor, $\text{C}_{33}=1/(\text{C}_{11}\text{C}_{22}-\text{C}_{12}^2)$ is determined as the consequence of the incompressibility condition, and $\otimes$ denotes dyadic tensor product. In addition, ϕ_{m}^{ξ} and $\phi_{\text{f}}^{\xi}=\phi_{\text{collagen}}^{\xi}+\phi_{\text{elastin}}^{\xi}$ are the layer-specific volume fractions of the matrix and effective fibers, respectively, determined from histological analysis data of the MVAL tissue as described in Section 2.4.

We assumed here that the matrix includes both non-fibrous substances and water, which is responsible for the low-tension (toe-region) response and the incompressibility of the planar tissue. It was also assumed that each layer has the same proportional mechanical response as those for the bulk MVAL tissue but varies in the microstructures, such as the material axial direction and fiber splay, and the layer-specific effective volume fractions of effective fibers and matrix ϕ_{f}^{ξ} and ϕ_{m}^{ξ}. As mentioned previously in Section 2.4, we employed a Gaussian distribution function with mean μ^{ξ} and standard deviation σ^{ξ} for the fiber angular orientation distribution function for each MVAL tissue layer

Author Manuscript Author Manuscript Author Manuscript Author Manuscript

$$\Gamma^{\xi}(\theta)=\frac{\exp\left[-\frac{(\theta-\mu^{\xi})^2}{2(\sigma^{\xi})^2}\right]}{\operatorname{erf}\left(\frac{\pi}{2\sqrt{2}\sigma^{\xi}}\right)\sqrt{2\pi}\sigma^{\xi}} \text{ with } \int_{-\pi/2}^{\pi/2}\Gamma^{\xi}(\theta)\mathrm{d}\theta=1. \quad (3)$$

Nodal displacements and elemental stress and strain fields were the primary output data from this level of the FE simulations. Tissue-level stretches along the circumferential and radial directions ($\overline{\lambda}_C$, $\overline{\lambda}_R$) were computed based on the in-plane strain tensor associated with the equi-biaxial stretching protocol described in Section 2.1. Tissue-level stretch in the transmural direction was then determined based on the incompressibility condition, i.e., $\overline{\lambda}_T=1/\overline{\lambda}_C\overline{\lambda}_R$. Numerically predictions were compared with experimental measurements to characterize material parameters c_0, c_1, and μ_m associated with the constitutive model in Eq. (1) for the bulk MVAL tissues by iteratively minimizing the error of the stretch-tension relationship between the FE simulation results and the experimental data. This procedure was automatically performed using an in-house MATLAB program that generates ABAQUS input file with updated parameters, executes FE simulations, extracts data from ABAQUS output database file, analyzes the stretch-tension responses, and performs parameter estimation with general-purpose nonlinear optimization technique.

2.5.2 FE modeling of the MVIC microenvironment—To explore the relative role of layer-specific ECM mechanical properties and microstructural composition on the layer-specific MVIC deformations, we developed the following finite element model of the MVIC microenvironment (Fig. 5-b). The MVIC microenvironment for each of the four layers was idealized as a representative area element (RAE) of 100 μm × 100 μm embedded with 37 uniformly distributed, horizontally aligned ellipsoidal inclusions. Here, we assumed that the size of the chosen RAE is relatively small, yet representative, on the circumferential-radial plane compared to the characteristic dimensions of the MVAL tissues, and the selected number of ellipsoidal inclusions was justified by the spatial distribution of MVICs in the leaflet based on our experimental observations. The MVIC geometry was simulated by an ellipsoidal inclusion with layer-specific dimensions based on the measurements from Section 2.3 (Table 1). The following considerations were made in this level of the FE simulations:

- **i.** Layer-specific ECM mechanical responses were modeled by a structural constitutive model similar to the one used for FE simulations of the MVAL tissue under equi-biaxial tension in Section 2.5.1 (c.f. Eq. (1)) with considerations of layer-specific volume fractions of non-fibrous matrix and collagenous fibers (ϕ_m^{ξ} and ϕ_f^{ξ}) and layer-specific preferred fiber direction as well as fiber splay ($\Gamma^{\xi}(\theta)$).
- **ii.** The MVIC mechanical responses were modeled by a Saint-Venant Kirchhoff material, which is an extension of the linear elastic model to the nonlinear, large-deformation regime:

$$\mathbf{S}^{\xi}_{\mathrm{MVIC}}=\lambda^{\xi}\mathrm{tr}(\mathbf{E})\mathbf{I}+2\mu^{\xi}\mathbf{E} \quad (4)$$

Author Manuscript Author Manuscript Author Manuscript Author Manuscript

where λ^{ξ} and μ^{ξ} are the material constants associated with each individual layer that can be related to the infinitesimal strain theory material constants E^{ξ} and ν^{ξ} ~0.5 using $E^{\xi} = \mu^{\xi}(3\lambda^{\xi} + 2\mu^{\xi})/(\lambda^{\xi} + \mu^{\xi})$ and $\nu^{\xi} = \lambda^{\xi}/2(\lambda^{\xi} + \mu^{\xi})$ (Simo and Hughes, 1998).

iii. The interfaces between the MVICs and MVAL ECM were assumed to be perfectly bonded with no interfacial debonding nor slipping (Huang et al., 2007), as illustrated in the transmission electron microscopy (TEM) image of the MVIC microenvironment in the fibrosa layer (Fig. 1-c).

iv. Consistent with related work on valvular tissues (Buchanan and Sacks, 2013), the MV leaflet tissue was considered as four *perfectly bonded* layers so that the layers were deformed homogeneously according to the tissue-level deformations. One plane-stress finite element RAE model was built for each layer, in which the thickness of the MVIC region for each layer was specified as the dimension of the third ellipsoidal axis based on the initial nuclear aspect ratio ($L_c=L_a*NAR_0$) and twice of this thickness was adopted for the MVAL ECM region. The typical RAE finite element model for the MVIC microenvironment has about 26,500 nodes and 26,600 elements.

v. Tissue-level stretches in the circumferential and radial directions ($\overline{\lambda}_C$, $\overline{\lambda}_R$), determined at the previous tissue-level FE simulation stage (Section 2.5.1), were applied as incremental nodal displacements on the four edges of the RAE model to mimic the tissue forces acting on the MVIC microenvironment.

Displacement and strain fields were the primary output from this level of FE modeling for the MVIC microenvironment. The parameter estimation described in Section 2.5.1 was employed to characterize the material constant of the MVIC for each of the four layers. In brief, the effective layer-specific MVIC NAR as a function of applied tension was computed based on the three principal stretches (λ_C, λ_R and $\lambda_T=1/\lambda_C\lambda_R$) averaging over the elements within each of the 37 ellipsoidal inclusions. The numerically predicted NAR-tension response was then compared to the experimental measurements, and layer-specific MVIC modulus E^{ξ} was determined by iteratively minimizing the difference between the numerical and experimental NAR-tension relationships.

3. Results

3.1 MVIC deformation analysis

The MVICs in the fibrosa and ventricularis layers had a noticeably larger deformation than those in the atrialis and spongiosa layers, reaching a NAR of 3.3 at the maximum physiological loading (Fig. 6). The deviations for each layer were large, indicating that there was a large amount of variation in deformation that the MVICs were experiencing in each layer. This discrepancy in the magnitude of layer-specific MVIC deformations may correspond to localized cell compaction due to different mechanisms of straightening and realigning of collagen and elastin fiber networks in each of the four layers, which ceased at the tension level of 25–30 N/m (Carruthers et al., 2012b). We also found that MVICs have an intrinsic ellipsoidal configuration with a NAR of ~2.5 at the unloaded state (T = 0 N/m).

Author Manuscript Author Manuscript Author Manuscript Author Manuscript

By comparing layer-specific MVIC orientation as a function of tension, we observed that reorientation occurs as a function of MVAL tissue layer (Fig. 7-a,b). This layer-specific discrepancy may be due to distinct microstructural compositions, ECM architecture, and the mismatch of material properties between the ECM, and MVIC for the four MVAL layers. At the unloaded state, the MVICs were not well oriented with large standard errors. At the maximum tension, the MVICs in the fibrosa and ventricularis layers oriented towards the circumferential direction, whereas the MVICs in the atrialis and spongiosa layers re-oriented towards the radial direction. As expected, the MVIC populations tend to re-orient along the preferred fiber direction of their respective layers (Carruthers et al., 2012b). Moreover, there was also reorientation of the MVIC population in the circumferential-radial plane, also referred to as in-plane deformation, except for the MVICs in the atrialis layer. This may correspond to the opposite directions of the collagen sheet orientation for the atrialis and fibrosa layers. *These findings suggest that MVIC deformation is more dependent on valvular layer structure than on the bulk tissue-level deformations*.

3.2 Finite element simulation results

The measured tissue-level stretches in the circumferential and radial directions gradually increased with applied loading (Fig. 8-a), with the circumferential stretch remaining almost constant beyond the level of ~30 N/m tissue-level tension and the radial stretch continued to increase monotonically. Numerical predictions of the tissue-level deformations matched the experimental data very well; at 150 N/m tension the numerically predicted tissue-level stretches were $\overline{\lambda}_{\mathrm{C}}^{\mathrm{FEM}}=1.177$ and $\overline{\lambda}_{\mathrm{R}}^{\mathrm{FEM}}=1.528$ in the circumferential and radial directions, respectively, whereas the experimental measurements were $\overline{\lambda}_{\mathrm{C}}^{\mathrm{EXP}}=1.16\pm0.04, \overline{\lambda}_{\mathrm{R}}^{\mathrm{EXP}}=1.52\pm0.16$.

As a further exploration of the interrelationships between tissue and cellular deformations, we directly applied the measured tissue-level deformations ($\overline{\lambda}_{\mathrm{C}}^{\mathrm{EXP}}, \overline{\lambda}_{\mathrm{R}}^{\mathrm{EXP}}, \overline{\lambda}_{\mathrm{T}}^{\mathrm{EXP}}$), assuming an ellipsoidal cellular geometry. In the calculation, we used this relation $\mathrm{NAR}_{\mathrm{Tension}}^{\mathrm{Fibrosa}}=(\overline{\lambda}_{\mathrm{C}}^{\mathrm{EXP}}/\overline{\lambda}_{\mathrm{T}}^{\mathrm{EXP}})\times\mathrm{NAR}_{0}^{\mathrm{Fibrosa}}$ to predict the NAR of the MVIC in the fibrosa layer. Clearly, the results from this simulation for the fibrosa layer deviated significantly from the experimental measurements (Fig. 8-b). This observation indicates that local MVIC deformations did not simply follow tissue-level deformations, although each layer was assumed to deform homogeneously with the MVAL bulk tissue. This result also reinforces the need for adopting the proposed macro-micro computational model for investigating local MVIC deformations induced from tissue-level forces.

Moreover, numerically predicted NARs from the FE simulations of the MVIC microenvironment decreased as the MVIC modulus increased for the four MVAL layers (Fig. 9a–d). This increase in MVIC modulus produced anisotropic changes in the MVIC deformations, i.e., five times larger of the MVIC modulus resulted in ~3% decrease in the circumferential stretch, ~12% decrease of the radial stretch, and ~16% increase of the transmural stretch at the maximum physiological loading of 150 N/m, leading to the observed reduction of the predicted NARs. The MVIC moduli for the four layers were characterized by matching the NAR-tension curves to the experimental measurements, and

Author Manuscript Author Manuscript Author Manuscript Author Manuscript

they were reported as follows: $E^{Atrialis}$=5.014 kPa, $E^{Spongiosa}$ =4.713 kPa, $E^{Fibrosa}$=5.348 kPa, and $E^{Ventricularis}$=5.167 kPa (Fig. 10a–d). These findings suggest that the MVICs may be phenotypically and biomechanically similar throughout the leaflet and more importantly that layer-specific local MVIC deformations in response to tissue-level mechanical stimuli are primarily controlled by each layer's respective structure and mechanical behavior rather than the intrinsic MVIC stiffness.

4. Discussion

4.1 Main findings

As in all soft tissues, the valvular ECM is a dynamic environment composed mainly of fibrous proteins that are continuously degraded and replaced. Perturbations to this system have been shown to be associated with aging and disease (Aikawa et al., 2006; Rabkin-Aikawa et al., 2004; Rabkin et al., 2001; Stephens et al., 2011; Stephens et al., 2010b). In order to better understand the mechanical behavior and remodeling of the MV, it is necessary to gain insight into MVIC mechanobiology, particularly on how MVIC biosynthesis is modulated by organ-level mechanical stimuli. Moreover, there is still a lack of understanding of how local forces are transduced to MVICs from tissue-level mechanical loading. Using MPM imaging and 3D image reconstruction, we demonstrated in this study that MVICs experience layer-specific deformations under controlled physiological biaxial tension loading. We also found that the MVICs in the fibrosa and ventricularis layers undergo larger deformations than the MVICs in the atrialis and spongiosa layers. Moreover, the MVICs in the atrialis layer are more likely to re-orient towards the radial direction in parallel to the collagen fibers in that layer, whereas the MVICs in the fibrosa layer tend to re-orient towards the circumferential direction in accordance with the collagen fiber direction in that layer.

These experimental observations were simulated in a macro-micro computational modeling framework that allowed linking tissue-level mechanical responses to the MVIC-ECM microenvironment. In general, the FE simulated MVIC NARs under tissue-level loading for four different layers were in fairly good agreement with the experimental measurements (Fig. 10a–d). On the other hand, the estimated MVIC NAR-tension response based on a simple affine transformation model and an ellipsoidal cellular geometry deviated significantly from the experimental data. The discrepancies were found to be due to the inability of this simple affine deformation model to capture the local MVIC behaviors. Thus, one important finding in the present study is that the MVICs act as distinct inclusions and do not simply deform convectively with the bulk tissue. Another important observation is that the MVIC moduli for all four layers were all within the range of 4.71–5.35 kPa. This suggests that layer-specific MVIC responses are primarily governed by layer-specific mechanical behaviors, which are a function of their microstructural compositions, level of anisotropy, and fiber architecture. The estimated MVIC moduli in this work also agreed reasonably with previous experimental measurements of heart valve interstitial cell stiffness, such as 0.3–0.5 kPa for fully deactivated VICs via the micropipette aspiration technique (Merryman et al., 2006b) and 50–60 kPa for highly activated VICs via atomic force microscope (Merryman et al., 2007).

Author Manuscript Author Manuscript Author Manuscript Author Manuscript

Both experimental measurements and numerical simulation results presented in this study indicate that MVIC deformation is dominated by layer-specific anisotropy and preferred fiber direction. This highlights the connection between organ-level loads and cellular deformations as a function of ECM fiber (mainly collagen and elastin) networks. In addition, from the parametric study of the effect of MVIC stiffness on the predicted NAR-tension response, we found that an increase in MVIC modulus leads to a relatively smaller decrease in MVIC stretches in both circumferential and radial directions compared to the larger decrease in the transmural stretch. As a result, the NAR-tension profile acquired from tissue-level responses becomes closer to the experimentally measured MVIC deformations (Fig. 9a–d). This suggests that the mechanical properties of both MVAL tissue and MVICs play an important role in accurate numerical modeling of the MVIC microenvironment in response to tissue-level mechanical stimuli.

4.2 Implications and comparisons with relevant research

As alluded to previously, it is essential to incorporate cell-level phenomena, such as protein biosynthesis and enzymatic degradation that affect tissue mechanical behaviors, into organ-level computation models for accurate simulations of the time course changes in heart valve function. It is also necessary to link cellular phenotypic and biophysical state to MV pathologies in order to fully understand how alterations in valve leaflet regional stresses and the induced mechanical stimuli lead to local changes in cellular mechanotransduction and mechanobiology and how those changes at the microscopic level, in turn, affect the subsequent adaption of tissue layer compositions and maintenance of overall tissue homeostasis. Although existing MV constitutive models (May-Newman and Yin, 1998; Prot et al., 2007; Sun and Sacks, 2005; Weinberg and Kaazempur-Mofrad, 2006; Weinberg and Kaazempur Mofrad, 2007) provide a rational basis for finite element simulations of MV mechanics, the underlying physiological changes that occur at the cellular level in response to tissue-level mechanical stimuli have not yet been included. Therefore, the present work is the first of its kind for investigating cellular behaviors in the MV leaflet tissues as a function of ECM architecture by considering the *driving forces* associated with layer-specific microstructural constituents, fiber architecture, and material anisotropy. In addition, the proposed integrated computational-experimental framework is applicable to other heart valves and can be implemented by incorporating appropriate leaflet tissue properties and utilizing the proposed real-time imaging technique to monitor VIC deformations under controlled physiological loading. These studies will also provide guidance for the design of the surgical repair procedures, through emulation of the biosynthetic and remodeling processes of the native, healthy heart valves.

The current findings show that although MVICs may be phenotypically similar in each layer, they experience different mechanical stimulatory inputs due to distinct ECM architecture and microstructure of the four MVAL tissue layers and may, as a result, secrete different ECM components. This further suggests a way to regulate tissue layer compositions by the VICs for achieving overall tissue homeostasis. In an earlier study on the aortic valve, serial histological section images were used to measure VIC deformations (Huang et al., 2007). A 2D representative volume area model of one homogeneous single fibrosa layer and a single aortic valve interstitial cell (AVIC) was developed. However,

Author Manuscript Author Manuscript Author Manuscript Author Manuscript

layer-specific microstructural compositions, fiber architecture and material anisotropy were not incorporated in the numerical modeling. Moreover, the predicted local AVIC and overall tissue peak stretches were 1.053/1.014 in the circumferential direction and 1.655/1.500 in the radial direction, showing that the AVIC almost follows tissue deformations; however, the MVIC and tissue-level peak stretches our model predicted were 1.126/1.188 in the circumferential direction and 1.127/1.422 in the radial direction, indicating that the MVIC are significantly different from the tissue-level deformations. Moreover, it was also found in the previous study on the semilunar heart valves (Carruthers et al., 2012a) that the NAR of the aortic VICs in the fibrosa layer reached a saturated value of 5.95 at the maximum transvalvular pressure, whereas the pulmonary VICs in the fibrosa layer underwent significantly greater changes in cellular deformation and reached a NAR of 9.66 at the maximum transvalvular pressure. While the underlying mechanobiology has not been fully understood, this observation along with the findings from this study suggest that the microenvironment of the fibrosa layer provides additional *stress shielding* for the VICs under high tissue stresses in the MV leaflets compared to those VICs in the semilunar heart valves.

Related ideas have been explored by other groups in the dynamic fluid-structure interaction simulations for studying aortic valve biomechanics (Weinberg and Mofrad, 2007; Weinberg and Kaazempur Mofrad, 2008; Weinberg et al., 2010). However, layer-specific microstructural compositions, fiber architecture, and material anisotropy were not fully considered in their tissue-level simulations, and the numerically predicted layer-specific VIC deformations were not validated with experimental data. Clearly, there still remains a need for quantitative data of layer-specific biosynthetic changes that occur in the MVIC microenvironment to be integrated into the development of a *bi-directional*, multi-scale finite element computational framework towards physiologically realistic modeling of MV function and pathophysiology.

4.3 FE model for the MVIC microenvironment

We further examined the appropriateness of the proposed FE model by comparing the predicted NARs of the MVICs residing in the fibrosa layer: (i) between a Saint-Venant Kirchhoff material as shown in Eq. (4) and a more commonly adopted neo-Hookean material in biomechanics research, $\mathbf{S}_{\mathrm{MVIC}}=\mu(\mathbf{I}-C_{33}\mathbf{C}^{-1})$, for the MVIC regions, and (ii) between 37 populated MVICs and a single MVIC (Table 3).

First, we noted in particular that the neo-Hookean material model even with a nonphysical value for μ of 2,000 kPa was not able to capture accurate MVIC mechanical response. The discrepancy in different material model forms could be explained by the nature of the stress-strain behaviors of these two material models, i.e., linearly increasing stress-strain curves for the Saint-Venant Kirchhoff material and concave stress-strain curves for the neo-Hookean material, under substantially large strain of ~15% for the MVICs. In addition, we observed from our numerical results that the 2D plane-stress formulation with the incompressibility condition automatically enforced is able to accurately predict both in-plane deformations (λ_T and λ_R) and the compaction in the transmural direction (λ_T), which faithfully mimics the real 3D ellipsoidal geometry and deformation of the MVICs. Furthermore, we also found in

Author Manuscript Author Manuscript Author Manuscript Author Manuscript

our numerical studies that the aligned angle of the cells and its in-plane rotation did not play a significant role in capturing the overall behavior of the MVICs, suggesting that the assumption of perfectly aligned ellipsoidal inclusions within the RAE model was a reasonable approximation in our FE simulations. Finally, the numerical predictions from the RAE model with 37 cells and from the model with a single cell at the center were not significantly different, since the cell volume fractions in both RAE models and the inclusion geometry and orientation are the same, leading to the same *homogenized* or *effective* RAE behaviors and properties, which are the averaged cell deformations in our case (Mura, 1987), based on the micromechanics theory as well as its extension for nonlinear materials and finite-strain regime using second-order homogenization techniques (Lopez-Pamies and Castaneda, 2004; Ponte Castaneda, 2002).

4.4 Relation to other tissues and VIC mechanotransduction

The ECM not only provides the tissue with its structural integrity, but it also influences cellular processes via three different mechanisms: (i) matricellular, in which the ECM signals through adhesion receptors, (ii) matricrine, which regulates the growth factor and cytokine expression in cells, and (iii) mechanical, which can be characterized as matrix elasticity or external forces (Chen and Simmons, 2011). The link between tissue-level mechanical responses, cellular deformations, and ECM remodeling is essential in understanding MV diseases and pathologies. A normal mechanical environment results in constant tissue structural integrity, whereas altered loading conditions may lead to dysfunction and disease. In cardiac muscle, cardiomyocytes have the ability to sense mechanical stimuli and convert themselves into intracellular growth signals, leading to hypertrophy (Sadoshima and Izumo, 1997). Similarly, the MV compensates for the ventricular remodeling, which typically occurs after left ventricular infarction, and becomes regurgitant (Dal-Bianco et al., 2009), while the MVICs have increased the α-SMA levels, indicating cellular activation.

The fundamental relationship between tissue- and cellular deformations has been investigated in other tissues, such as tendon, ligament, bone and cartilage repair. Soslowsky studied tendons at both tissue and cellular levels (Dunkman et al., 2013a; Dunkman et al., 2013b) and demonstrated that aged patellar tendons result in changes in the functional activity, tissue architecture, tenocyte shape, and collagen fiber alignment. These changes were found to be regulated by ECM proteoglycans (PGs), decorin and biglycan, which have a decreased expression in aged tendons (Robinson et al., 2004; Robinson et al., 2005). Similarly, mechanical stimuli were found to alter the homeostatic balance between collagen biosynthesis and catabolism. Guilak investigated the effects of static and dynamic compression on the meniscal cell gene expression and found that types I and II collagen fibers as well as decorin are regulated by common mechanical stimuli (Upton et al., 2003).

VICs sense and transduce extracellular mechanical stimuli, such as stretch, shear stress and pressure, into intracellular biomechanical signals directly and indirectly through several mechanisms that include receptors, ion channels, caveolin, G proteins, cell cytoskeleton, kinases, and transcriptional factors (Li and Xu, 2000). These signals are processed and sorted by molecules on the cell surface, resulting in the cell response by a network of

Author Manuscript Author Manuscript Author Manuscript Author Manuscript

intracellular signaling pathways. Mechanical stimuli were found to activate the mitogen-activated-protein (MAP) kinase pathway, which controls gene expression (Schmidt et al., 1998). Integrins, which are the signal receptors that physically link the cell surface to the surrounding ECM, play an important role in cellular mechanotransduction, particularly in response to physiological and pathophysiological signals.

Mechanical forces modulate cell physiology and affect the biosynthetic activities of cells in the tissue. In many valve pathologies, significantly altered profiles of ECM components accompany the alterations in the mechanical strains within the tissues (Grande-Allen et al., 2003; Quick et al., 1997; Stephens et al., 2008). These measured differences initiated numerous in-vitro studies to fully characterize and link tissue-level deformation to cellular response. Static and cyclic tissue strains can profoundly influence the phenotypic and biosynthetic responses of VICs *in vitro* and modulate cell function through the biosynthesis of glycosaminoglycans and proteoglycans (Gupta and Grande-Allen, 2006; Gupta et al., 2009), an increase in α-SMA expression and non-muscle embryonic myosin (Lacerda et al., 2012), and the degradation of extracellular matrix components by proteolytic enzymes, matrix metalloproteases (MMP), tissue inhibitors of MMPs, and cathepsins. These changes indicate an enhancement of the activated and contractile phenotype of VICs (Balachandran et al., 2009a; Balachandran et al., 2006a) and can further lead to cellular proliferation and apoptosis that are typically responsible for valve degeneration and disease.

Collectively, these studies suggest the substantial effect of tissue-induced cellular deformations on the regulation of VIC mechano-biological responses. Moreover, excessive tissue stresses caused by surgical repair of the MV can lead to microstructural and cellular changes that in turn, affect the long-term durability of valve repair (Gillinov et al., 2001). There is thus a need to fully understand and link organ-level deformations to the biosynthetic changes that occur at the cellular level. This will enable the development of multi-scale approaches to tissue modeling for better understanding of the relation between MVIC deformation and biosynthetic state that is important in maintaining overall tissue homeostasis. Understanding this functional relation will be helpful for elucidating valvular pathologies, and will eventually lead to a more reasonable basis for the design of improved surgical repair procedures.

4.5 Limitations

The performed FE simulations were based on experimental data collected in viable valve tissues. While we have shown that our hypothermosol preparation maintains cell viability (Merryman et al., 2004; Merryman et al., 2009; Merryman et al., 2006c), the present technique required fixation of the tissue at various loaded states. It is possible that during this process some additional deformation occurred, although no detectable changes in specimen dimensions were observed in the experiments. Regardless, such additional deformations if they exist, would be systematic and would not appreciably affect the present results.

Next, it was assumed in the FE simulations of the MVIC microenvironment that the MVAL ECM region was modeled using a similar constitutive model form to the one for the MVAL tissues with considerations of the known preferred fiber directions, mass fractions of ECM

Author Manuscript Author Manuscript Author Manuscript Author Manuscript

and fibers, and the measured level of fiber alignment in each of the four layers. A more realistic layer-specific constitutive model may be adopted as future extensions once the data of the mechanical responses of each separated layer for the MV leaflet tissues, similar to the work for the aortic valve tissue (Stella and Sacks, 2007), becomes available. Moreover, the stress-strain behavior was simplified by using an effective fiber representation in the structural constitutive model. Further information may be incorporated to develop a full-blown structural constitutive model, which accounts for the contributions of elastin fibers and collagen fibers separately. Nevertheless, adopting the current structural constitutive model for the MVAL ECM yielded good predictions of local MVIC deformations compared to our measurements for all four layers, indicating that the above assumptions in the FE simulations served as a reasonable approximation.

Finally, the structural model can provides valuable insight into tissue function by integrating the microscopic fiber structure, kinematics, and structural adaptions into the stress-strain behaviors. This stands in contrast to conventional invariant-based constitutive models (May-Newman and Yin, 1998; Prot et al., 2007) and Fung-type constitutive models (Fung, 1993), which are phenomenological models whose parameters lack physical meanings. Despite these advantages, issues associated with efficient numerical integration of the fiber-splay in Eq. (1) still remains and may limit its applications to large-scale modeling of soft tissue and related tissue biomaterials. To address this in the present work, we constructed a global array at the pre-calculation stage in ABAQUS UMAT which stores all necessary information about the numerical integration, including fiber angle θ_j, integration weight w_j, and its respective values of fiber angular distribution function $\Gamma(\theta_j)$, and trigonometric functions for computing **N** vector and **N**⊗**N** matrix for all 100 Gauss quadrature points between $-\pi/2$ and $\pi/2$. The CPU time for simulating the MVIC microenvironment using this implementation was significantly reduced by ~30% compared to the direct implementation, which computes those values for each Gauss quadrature point at runtime. The computational efficiency can be further improved by carrying out the close-form expression for the integral in Eq. (1) similar to the previous work for the π-periodic von Mises fiber distribution (Raghupathy and Barocas, 2009). However, such extensions are limited to simple forms and cannot account for the increasing complex microstructures currently being developed in our lab that will be presented in the forthcoming publications.

4.6 Summary

In the present study, we employed an integrated computational-experimental approach to quantify and simulate layer-specific cellular deformations across the MV anterior leaflet tissue under controlled physiological tension loading. The similarity of predicted MVIC mechanical properties suggests a similar phenotypic state for the VICs regardless of layer location, and potentially a similar homeostatic state for all layers as well. These results underscore the essential role played by layer-specific microstructural compositions and fiber architecture in the underlying MVIC deformations. This work can be utilized to provide insightful information about MV function and behavior across multiple length scales in response to mechanical stimuli, specifically, the stress overload induced by mitral valve disease and surgical repair, and eventually to investigate the effect of cellular deformations on collagen biosynthesis. This important piece of information can in turn, be used to

Author Manuscript Author Manuscript Author Manuscript Author Manuscript

establish the interrelationship between cellular deformations and tissue-level mechanical behaviors that maintains the homeostasis of the functioning MV. The proposed macro-micro computational framework will be beneficial in the future when integrated with organ-level, structurally accurate finite element models to investigate MV pathophysiology and disease progression as a function of MVIC mechanobiology and ECM architecture, and ultimately to improve MV surgical repair procedures by enhancing the long-term durability.

Acknowledgments

The assistance from Dr. Simon C. Watkins and Greg Gibson for the multi-photon microscope and Bryan Good for design and development of the mini-biaxial device is greatly appreciated. This work is funded by the National Institutes for Health (NIH) grants R01 HL119297, HL63954, HL103723 and HL73021. Dr. Chung-Hao Lee is supported in part by an ICES Postdoctoral Fellowship and the American Heart Association Southwest Affiliate Postdoctoral Fellowship 14POST18160013. Dr. Christopher A. Carruthers was partially supported by the NIH grant 5T32EB003392 and a National Science Foundation (NSF) Graduate Research Fellowship.

References

Aikawa E, Whittaker P, Farber M, Mendelson K, Padera RF, Aikawa M, Schoen FJ. Human semilunar cardiac valve remodeling by activated cells from fetus to adult: implications for postnatal adaptation, pathology, and tissue engineering. Circulation. 2006; 113:1344–1352. [PubMed: 16534030]

Bairati A, DeBiasi S. Presence of a smooth muscle system in aortic valve leaflets. Anat Embryol. 1981; 161:329–340. [PubMed: 7187826]

Balachandran K, Sucosky P, Jo H, Yoganathan A. Elevated cyclic stretch alters matrix remodeling in aortic valve cusps: implications for degenerative aortic valve disease. Am J Physiol Heart Circ Physiol. 2009a; 296:H756–H764. [PubMed: 19151254]

Balachandran K, Sucosky P, Jo H, Yoganathan AP. Elevated cyclic stretch alters matrix remodeling in aortic valve cusps: implications for degenerative aortic valve disease. American Journal of Physiology-Heart and Circulatory Physiology. 2009b; 296:H756–H764. [PubMed: 19151254]

Balachandran K, Konduri S, Sucosky P, Jo H, Yoganathan A. An Ex Vivo Study of the Biological Properties of Porcine Aortic Valves in Response to Circumferential Cyclic Stretch. Annals of Biomedical Engineering. 2006a; 34:1655–1665. [PubMed: 17031600]

Balachandran K, Konduri S, Sucosky P, Jo H, Yoganathan A. An ex vivo study of the biological properties of porcine aortic valves in response to circumferential cyclic stretch. Annals of biomedical engineering. 2006b; 34:1655–1665. [PubMed: 17031600]

Buchanan RM, Sacks MS. Interlayer micromechanics of the aortic heart valve leaflet. Biomech Model Mechanobiol. 2013 In Press, doi:10.1007/s10237-013-0536-6.

Carruthers CA, Alfieri CM, Joyce EM, Watkins SC, Yutzey KE, Sacks MS. Gene Expression and Collagen Fiber Micromechanical Interactions of the Semilunar Heart Valve Interstitial Cell. Cellular and Molecular Bioengineering. 2012a; 5:254–265. [PubMed: 23162672]

Carruthers, CA.; Good, B.; D'Amore, A.; Liao, J.; Amini, R.; Watkins, SC.; Sacks, MS. Alterations in the microstructure of the anterior mitral valve leaflet under physiological stress. ASME 2012 Summer Bioengineering Conference; American Society of Mechanical Engineers; 2012b. p. 227-228.

Chen JH, Simmons CA. Cell-matrix interactions in the pathobiology of calcific aortic valve disease: critical roles for matricellular, matricrine, and matrix mechanics cues. Circ Res. 2011; 108:1510–1524. [PubMed: 21659654]

Chuong CJ, Fung YC. On residual stresses in arteries. J Biomech Eng. 1986; 108:189–192. [PubMed: 3079517]

D'Amore, A.; Stella, JA.; Schmidt, DE.; Wagner, WR.; Sacks, MS. Micro-Meso Scale Model of Electrospun Poly (Ester Urethane) Urea Scaffolds. Proceedings of the ASME 2009 Summer Bioengineering Conference; Lake Tahoe, CA. 2009.

Author Manuscript Author Manuscript Author Manuscript Author Manuscript

Dal-Bianco JP, Aikawa E, Bischoff J, Guerrero JL, Handschumacher MD, Sullivan S, Johnson B, Titus JS, Iwamoto Y, Wylie-Sears J, Levine RA, Carpentier A. Active adaptation of the tethered mitral valve: insights into a compensatory mechanism for functional mitral regurgitation. Circulation. 2009; 120:334–342. [PubMed: 19597052]

Dunkman AA, Buckley MR, Mienaltowski MJ, Adams SM, Thomas SJ, Kumar A, Beason DP, Iozzo RV, Birk DE, Soslowsky LJ. The injury response of aged tendons in the absence of biglycan and decorin. Matrix Biology. 2013a In Press.

Dunkman AA, Buckley MR, Mienaltowski MJ, Adams SM, Thomas SJ, Satchell L, Kumar A, Pathmanathan L, Beason DP, Iozzo RV. Decorin expression is important for age-related changes in tendon structure and mechanical properties. Matrix Biology. 2013b; 32:3–13. [PubMed: 23178232]

Einstein DR, Kunzelman KS, Reinhall PG, Cochran RP, Nicosia MA. Haemodynamic determinants of the mitral valve closure sound: a finite element study. Med Biol Eng Comput. 2004; 42:832–846. [PubMed: 15587476]

El-Hamamsy I, Balachandran K, Yacoub MH, Stevens LM, Sarathchandra P, Taylor PM, Yoganathan AP, Chester AH. Endothelium-dependent regulation of the mechanical properties of aortic valve cusps. Journal of the American College of Cardiology. 2009; 53:1448–1455. [PubMed: 19371829]

Fan R, Sacks MS. Simulation of planar soft tissues using a structural constitutive model: finite element implementation and validation. J Biomech. 2014 In Press.

Fata B, Carruthers CA, Gibson G, Watkins SC, Gottlieb D, Mayer JE, Sacks MS. Regional structural and biomechanical alterations of the ovine main pulmonary artery during postnatal growth. J Biomech Eng. 2013; 135:021022. [PubMed: 23445067]

Filip DA, Radu A, Simionescu M. Interstitial cells of the heart valve possess characteristics similar to smooth muscle cells. Circulation Research. 1986; 59:310–320. [PubMed: 3769149]

Flanagan TC, Black A, O'Brien M, Smith TJ, Pandit AS. Reference Models for Mitral Valve Tissue Engineering Based on Valve Cell Phenotype and Extracellular Matrix Analysis. Cells Tissues Organs. 2006; 183:12–23. [PubMed: 16974091]

Fung YC. What are the residual stresses doing in our blood vessels? Ann Biomed Eng. 1991; 19:237–249. [PubMed: 1928868]

Fung, YC. Biomechanics: Mechanical Properties of Living Tissues. Springer Verlag: New York; 1993.

Fung YC, Liu SQ. Changes of zero-stress state of rat pulmonary arteries in hypoxic hypertension. J Appl Physiol. 1991; 70:2455–2470. [PubMed: 1885439]

Gillinov AM, Wierup PN, Blackstone EH, Bishay ES, Cosgrove DM, White J, Lytle BW, McCarthy PM. Is repair preferable to replacement for ischemic mitral regurgitation? J Thorac Cardiovasc Surg. 2001; 122:1125–1141. [PubMed: 11726887]

Grande-Allen K, Liao J. The heterogeneous biomechanics and mechanobiology of the mitral valve: implications for tissue engineering. Curr Cardiol Rep. 2011; 13:113–120. [PubMed: 21221857]

Grande-Allen KJ, Griffin BP, Ratliff NB, Cosgrove DM, Vesely I. Glycosaminoglycan profiles of myxomatous mitral leaflets and chordae parallel the severity of mechanical alterations. J Am Coll Cardiol. 2003; 42:271–277. [PubMed: 12875763]

Gupta V, Grande-Allen KJ. Effects of static and cyclic loading in regulating extracellular matrix synthesis by cardiovascular cells. Cardiovasc Res. 2006; 72:375–383. [PubMed: 17010955]

Gupta V, Werdenberg JA, Mendez JS, Grande-Allen KJ. Influence of strain on proteoglycan synthesis by valvular interstitial cells in 3D culture. Acta Biomaterialia. 2007; 4:88–96. [PubMed: 17928282]

Gupta V, Tseng H, Lawrence BD, Jane Grande-Allen K. Effect of cyclic mechanical strain on glycosaminoglycan and proteoglycan synthesis by heart valve cells. Acta biomaterialia. 2009; 5:531–540. [PubMed: 19004676]

Huang HY, Liao J, Sacks MS. In-situ deformation of the aortic valve interstitial cell nucleus under diastolic loading. J Biomech Eng. 2007; 129:880–889. [PubMed: 18067392]

Konduri S, Xing Y, Warnock JN, He Z, Yoganathan AP. Normal physiological conditions maintain the biological characteristics of porcine aortic heart valves: an ex vivo organ culture study. Ann Biomed Eng. 2005; 33:1158–1166. [PubMed: 16133923]

Author Manuscript Author Manuscript Author Manuscript Author Manuscript

Kunzelman KS, Einstein DR, Cochran RP. Fluid-structure interaction models of the mitral valve: function in normal and pathological states. Philos Trans R Soc Lond B Biol Sci. 2007; 362:1393–1406. [PubMed: 17581809]

Kunzelman KS, Cochran RP, Murphree SS, Ring WS, Verrier ED, Eberhart RC. Differential collagen distribution in the mitral valve and its influence on biomechanical behaviour. J Heart Valve Dis. 1993; 2:236–244. [PubMed: 8261162]

Lacerda CM, Kisiday J, Johnson B, Orton EC. Local serotonin mediates cyclic strain-induced phenotype transformation, matrix degradation, and glycosaminoglycan synthesis in cultured sheep mitral valves. American Journal of Physiology-Heart and Circulatory Physiology. 2012; 302:H1983–H1990. [PubMed: 22345569]

Lanir Y. Mechanisms of residual stress in soft tissues. J Biomech Eng. 2009; 131:044506. [PubMed: 19275448]

Lee CH, Amini R, Gorman RC, Gorman JH 3rd, Sacks MS. An inverse modeling approach for stress estimation in mitral valve anterior leaflet valvuloplasty for in-vivo valvular biomaterial assessment. J Biomech. 2014; 47:2055–2063. [PubMed: 24275434]

Li C, Xu Q. Mechanical stress-initiated signal transductions in vascular smooth muscle cells. Cellular signalling. 2000; 12:435–445. [PubMed: 10989277]

Liu SQ, Fung YC. Relationship between hypertension, hypertrophy, and opening angle of zero-stress state of arteries following aortic constriction. J Biomech Eng. 1989; 111:325–335. [PubMed: 2486372]

Lopez-Pamies O, Castaneda PP. Second-order homogenization estimates incorporating field fluctuations in finite elasticity. Mathematics and Mechanics of Solids. 2004; 9:243–270.

Mansi T, Voigt I, Georgescu B, Zheng X, Mengue EA, Hackl M, Ionasec RI, Noack T, Seeburger J, Comaniciu D. An integrated framework for finite-element modeling of mitral valve biomechanics from medical images: Application to MitralClip intervention planning. Medical image analysis. 2012; 16:1330–1346. [PubMed: 22766456]

May-Newman K, Yin FC. A constitutive law for mitral valve tissue. J Biomech Eng. 1998; 120:38–47. [PubMed: 9675679]

Merryman, WD.; Youn, I.; Guilak, F.; Sacks, MS. Contractile abilities of the aortic valve leaflet interstitial cell; Biomedical Engineering Society (BMES) Annual Fall Meeting; Philadelphia, PA. 2004.

Merryman WD, Huang HYS, Schoen FJ, Sacks MS. The effects of cellular contraction on aortic valve leaflet flexural stiffness. J Biomech. 2006a; 39:88–96. [PubMed: 16271591]

Merryman WD, Bieniek PD, Guilak F, Sacks MS. Viscoelastic properties of the aortic valve interstitial cell. J Biomech Eng. 2009; 131:041005. [PubMed: 19275434]

Merryman WD, Liao J, Parekh A, Candiello JE, Lin H, Sacks MS. Differences in tissue-remodeling potential of aortic and pulmonary heart valve interstitial cells. Tissue Eng. 2007; 13:2281–2289. [PubMed: 17596117]

Merryman WD, Youn I, Lukoff HD, Krueger PM, Guilak F, Hopkins RA, Sacks MS. Correlation between heart valve interstitial cell stiffness and transvalvular pressure: implications for collagen biosynthesis. Am J Physiol Heart Circ Physiol. 2006b; 59:H224–H231. [PubMed: 16126816]

Merryman WD, Youn I, Lukoff HD, Krueger PM, Guilak F, Hopkins RA, Sacks MS. Correlation between heart valve interstitial cell stiffness and transvalvular pressure: implications for collagen biosynthesis. Am J Physiol Heart Circ Physiol. 2006c; 290:H224–H231. [PubMed: 16126816]

Messier RH Jr, Bass BL, Aly HM, Jones JL, Domkowski PW, Wallace RB, Hopkins RA. Dual structural and functional phenotypes of the porcine aortic valve interstitial population: characteristics of the leaflet myofibroblast. J Surg Res. 1994; 57:1–21. [PubMed: 8041124]

Mulholland DL, Gotlieb AI. Cell biology of valvular interstitial cells. Canadian J Cardiology. 1996; 12:231–236.

Mura, T. Micromechanics of defects in solids. Springer: 1987.

Ogden, R. Nonlinear elasticity, anisotropy, material stability, and residual stresses in soft tissue. In: Ogden, R., editor. Biomechanics of soft tissue in cardiovascular system. Springer: New York; 2003.

Author Manuscript Author Manuscript Author Manuscript Author Manuscript

Ponte Castañeda P. Second-order homogenization estimates for nonlinear composites incorporating field fluctuations: I—theory. Journal of the Mechanics and Physics of Solids. 2002; 50:737–757.

Prot V, Skallerud B. Nonlinear solid finite element analysis of mitral valves with heterogeneous leaflet layers. Comput Mech. 2009; 43:353–368.

Prot V, Skallerud B, Holzapfel G. Transversely isotropic membrane shells with application to mitral valve mechanics. Constitutive modelling and finite element implementation. Int J Numer Methods Eng. 2007; 71:987–1008.

Quick DW, Kunzelman KS, Kneebone JM, Cochran RP. Collagen synthesis is upregulated in mitral valves subjected to altered stress. Asaio J. 1997; 43:181–186. [PubMed: 9152488]

Rabkin-Aikawa E, Farber M, Aikawa M, Schoen FJ. Dynamic and reversible changes of interstitial cell phenotype during remodeling of cardiac valves. J Heart Valve Dis. 2004; 13:841–847. [PubMed: 15473488]

Rabkin E, Hoerstrup SP, Aikawa M, Mayer JE Jr, Schoen FJ. Evolution of cell phenotype and extracellular matrix in tissue-engineered heart valves during in-vitro maturation and in-vivo remodeling. J Heart Valve Dis. 2002; 11:308–314. discussion 314. [PubMed: 12056720]

Rabkin E, Aikawa M, Stone JR, Fukumoto Y, Libby P, Schoen FJ. Activated interstitial myofibroblasts express catabolic enzymes and mediate matrix remodeling in myxomatous heart valves. Circulation. 2001; 104:2525–2532. [PubMed: 11714645]

Raghupathy R, Barocas VH. A closed-form structural model of planar fibrous tissue mechanics. J Biomech. 2009; 42:1424–1428. S0021-9290(09)00202-4 [pii]. [PubMed: 19457487]

Rausch MK, Famaey N, Shultz TO, Bothe W, Miller DC, Kuhl E. Mechanics of the mitral valve : a critical review, an in vivo parameter identification, and the effect of prestrain. Biomech Model Mechanobiol. 2012; 12:1053–1071. [PubMed: 23263365]

Robinson PS, Derwin KA, Iozzo RV, Soslowsky LJ, Lin TW, Reynolds PR. Strain-rate sensitive mechanical properties of tendon fascicles from mice with genetically engineered alterations in collagen and decorin. J Biomech Eng. 2004; 126:252–257. [PubMed: 15179856]

Robinson PS, Huang T-F, Kazam E, Iozzo RV, Soslowsky LJ, Birk DE. Influence of decorin and biglycan on mechanical properties of multiple tendons in knockout mice. J Biomech Eng. 2005; 127:181–185. [PubMed: 15868800]

Ruifrok AC, Johnston DA. Quantification of histochemical staining by color deconvolution. Analytical and quantitative cytology and histology/the International Academy of Cytology [and] American Society of Cytology. 2001; 23:291–299.

Sacks M. Biaxial mechanical evaluation of planar biological materials. Journal of Elasticity. 2000; 61:199–246.

Sacks MS, Yoganathan AP. Heart valve function: a biomechanical perspective. Philos Trans R Soc Lond B Biol Sci. 2008; 363:1369–1391. [pii] 10.1098/rstb.2008.0062.

Sacks MS, Smith DB, Hiester ED. A small angle light scattering device for planar connective tissue microstructural analysis. Ann Biomed Eng. 1997; 25:678–689. [PubMed: 9236980]

Sacks MS, Merryman WD, Schmidt DE. On the biomechanics of heart valve function. J Biomech. 2009; 42:1804–1824. [pii] 10.1016/j.jbiomech.2009.05.015. [PubMed: 19540499]

Sacks MS, Enomoto Y, Graybill JR, Merryman WD, Zeeshan A, Yoganathan AP, Levy RJ, Gorman RC, Gorman JH 3rd. In-vivo dynamic deformation of the mitral valve anterior leaflet. Ann Thorac Surg. 2006; 82:1369–1377. [PubMed: 16996935]

Sadoshima J, Izumo S. The cellular and molecular response of cardiac myocytes to mechanical stress. Annual review of physiology. 1997; 59:551–571.

Schmidt C, Pommerenke H, Dürr F, Nebe B, Rychly J. Mechanical stressing of integrin receptors induces enhanced tyrosine phosphorylation of cytoskeletally anchored proteins. Journal of Biological Chemistry. 1998; 273:5081–5085. [PubMed: 9478959]

Simo, JC.; Hughes, TJR. Computational inelasticity. Springer: New York; 1998.

Skallerud B, Prot V, Nordrum IS. Modeling active muscle contraction in mitral valve leaflets during systole: a first approach. Biomech Model Mechanobiol. 2011; 10:11–26. [PubMed: 20419330]

Smith S, Taylor PM, Chester AH, Allen SP, Dreger SA, Eastwood M, Yacoub MH. Force generation of different human cardiac valve interstitial cells: relevance to individual valve function and tissue engineering. Journal of Heart Valve Disease. 2007; 16:440. [PubMed: 17702371]

Author Manuscript Author Manuscript Author Manuscript Author Manuscript

Stella JA, Sacks MS. On the biaxial mechanical properties of the layers of the aortic valve leaflet. J Biomech Eng. 2007; 129:757–766. [PubMed: 17887902]

Stephens E, Durst C, Swanson J, Grande-Allen K, Ingels N, Miller D. Functional coupling of valvular interstitial cells and collagen via α2β1 integrins in the mitral leaflet. Cellular and Molecular Bioeng. 2010a; 3:428–437.

Stephens EH, Durst CA, West JL, Grande-Allen KJ. Mitral valvular interstitial cell responses to substrate stiffness depend on age and anatomic region. Acta Biomaterialia. 2011; 7:75–82. [PubMed: 20624493]

Stephens EH, de Jonge N, McNeill MP, Durst CA, Grande-Allen KJ. Age-Related Changes in Material Behavior of Porcine Mitral and Aortic Valves and Correlation to Matrix Composition. Tissue Engineering Part A. 2010b; 16:867–878. doi: [PubMed: 19814589]

Stephens EH, Nguyen TC, Itoh A, Ingels NB, Miller DC, Grande-Allen KJ. The Effects of Mitral Regurgitation Alone Are Sufficient for Leaflet Remodeling. Circulation. 2008; 118:S243–S249. [PubMed: 18824762]

Stephens EH, Timek TA, Daughters GT, Kuo JJ, Patton AM, Baggett LS, Ingels NB, Miller DC, Grande-Allen KJ. Significant changes in mitral valve leaflet matrix composition and turnover with tachycardia-induced cardiomyopathy. Circulation. 2009; 120:S112–S119. [PubMed: 19752355]

Stevanella M, Maffessanti F, Conti CA, Votta E, Arnoldi A, Lombardi M, Parodi O, Caiani EG, Redaelli A. Mitral valve patient-specific finite element modeling from cardiac MRI: application to an annuloplasty procedure. Cardiovas Eng Tech. 2011; 2:66–76.

Sun W, Sacks MS. Finite element implementation of a generalized Fung-elastic constitutive model for planar soft tissues. Biomech Model Mechanobiol. 2005

Taber LA, Humphrey JD. Stress-modulated growth, residual stress, and vascular heterogeneity. J Biomech Eng. 2001; 123:528–535. [PubMed: 11783722]

Taylor PM, Batten P, Brand NJ, Thomas PS, Yacoub MH. The cardiac valve interstitial cell. Int J Biochem Cell Biol. 2003; 35:113–118. [PubMed: 12479860]

Upton ML, Chen J, Guilak F, Setton LA. Differential effects of static and dynamic compression on meniscal cell gene expression. Journal of orthopaedic research. 2003; 21:963–969. [PubMed: 14554206]

Votta E, Caiani E, Veronesi F, Soncini M, Montevecchi FM, Redaelli A. Mitral valve finite-element modelling from ultrasound data: a pilot study for a new approach to understand mitral function and clinical scenarios. Philos Transact A Math Phys Eng Sci. 2008; 366:3411–3434.

Wang Q, Sun W. Finite Element Modeling of Mitral Valve Dynamic Deformation Using Patient-Specific Multi-Slices Computed Tomography Scans. Ann Biomed Eng. 2013; 41:142–153. [PubMed: 22805982]

Watkins, S. Immunohistochemistry. Current Protocols in Cytometry: John Wiley & Sons, Inc.; 2001.

Weinberg EJ, Kaazempur-Mofrad MR. A large-strain finite element formulation for biological tissues with application to mitral valve leaflet tissue mechanics. J Biomech. 2006; 39:1557–1561. [PubMed: 16038913]

Weinberg EJ, Mofrad MRK. Transient, three-dimensional, multiscale simulations of the human aortic valve. Cardiovascular Engineering. 2007; 7:140–155. [PubMed: 18026835]

Weinberg EJ, Kaazempur Mofrad MR. A finite shell element for heart mitral valve leaflet mechanics, with large deformations and 3D constitutive material model. J Biomech. 2007; 40:705–711. [PubMed: 16574127]

Weinberg EJ, Kaazempur Mofrad MR. A multiscale computational comparison of the bicuspid and tricuspid aortic valves in relation to calcific aortic stenosis. Journal of biomechanics. 2008; 41:3482–3487. [PubMed: 18996528]

Weinberg EJ, Shahmirzadi D, Mofrad MRK. On the multiscale modeling of heart valve biomechanics in health and disease. Biomechanics and modeling in mechanobiology. 2010; 9:373–387. [PubMed: 20066464]

Wenk JF, Zhang Z, Cheng G, Malhotra D, Acevedo-Bolton G, Burger M, Suzuki T, Saloner DA, Wallace AW, Guccione JM, Ratcliffe MB. First finite element model of the left ventricle with mitral valve: insights into ischemic mitral regurgitation. Ann Thorac Surg. 2010; 89:1546–1553. [PubMed: 20417775]

Author Manuscript Author Manuscript Author Manuscript Author Manuscript

Wyss K, Yip CY, Mirzaei Z, Jin X, Chen J-H, Simmons CA. The elastic properties of valve interstitial cells undergoing pathological differentiation. Journal of Biomechanics. 2012; 45:882–887. [PubMed: 22189247]

Author Manuscript Author Manuscript Author Manuscript Author Manuscript

Highlights

- Layer-specific local MVICs do not simply follow MVAL bulk tissue deformations
- Cellular deformations are a function of the ECM collagen and elastin fiber networks
- ECM & MVIC properties are critical for accurate modeling the MVIC microenvironment

Author Manuscript Author Manuscript Author Manuscript Author Manuscript

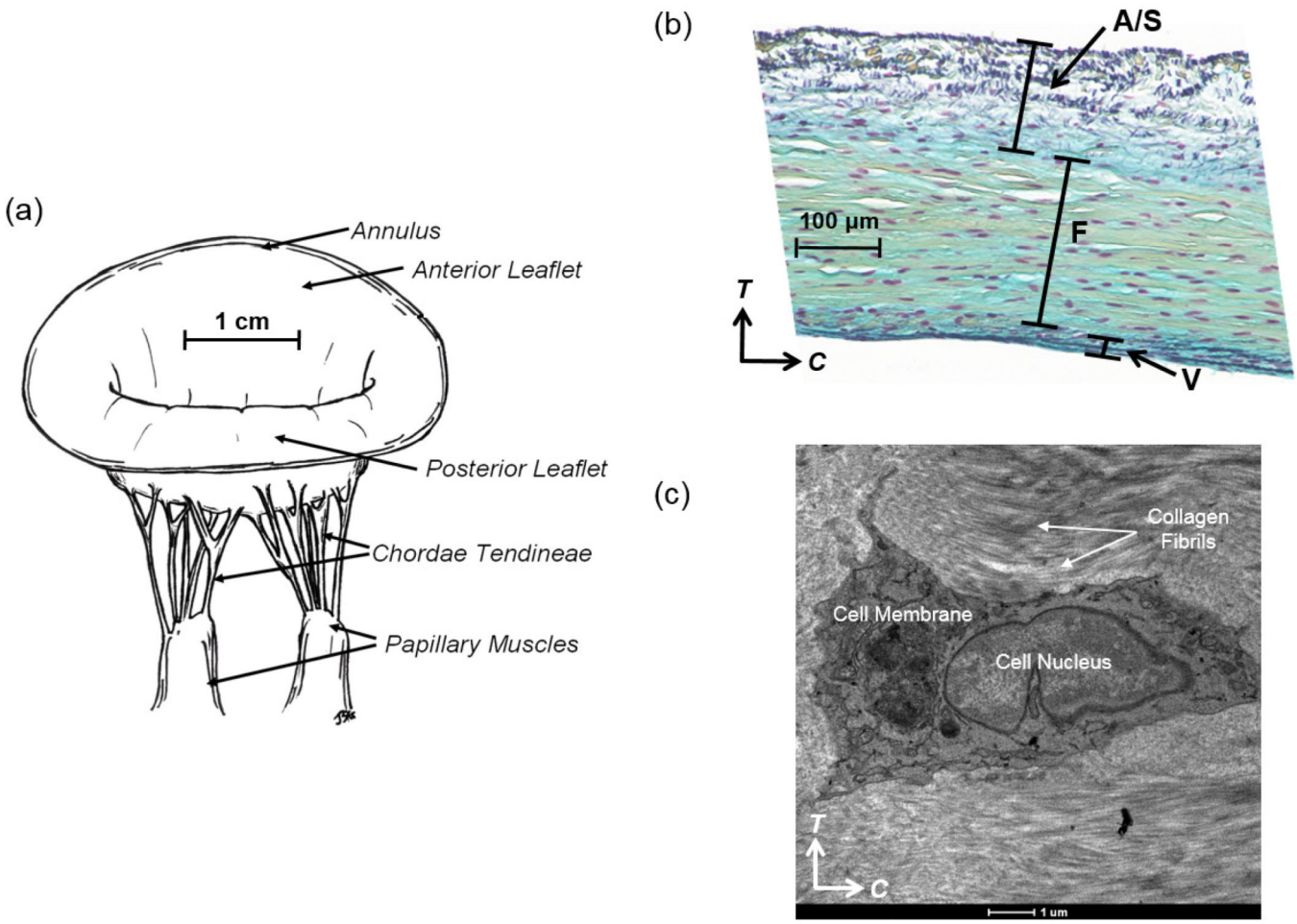

Figure 1.

(a) Illustrative diagram of the native ovine mitral valve, demonstrating key anatomical components: two main leaflets (anterior leaflet and posterior leaflet), annulus, chordae tendineae and papillary muscles, (b) stained histologic image showing four-layered structure of the MV tissue (A: atrialis, S: spongiosa, F: fibrosa, V: ventricularis), and (c) transmission electron microscopy (TEM) image of the intact MVIC residing in the fibrosa layer of the MVAL, showing the MVIC microenvironment and its alignment with the collagen fibrils in the circumferential direction (scale bar=1 μm, C: circumferential direction, and T: transmural direction).

Author Manuscript Author Manuscript Author Manuscript Author Manuscript

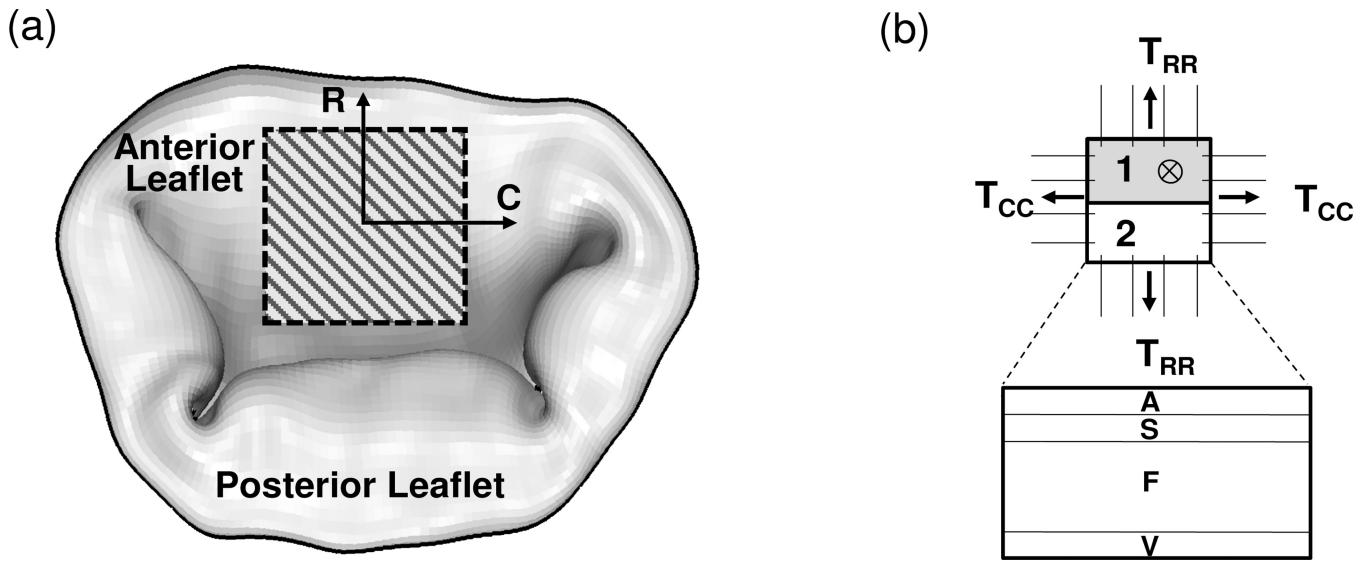

Figure 2.

Schematic diagrams of (a) ovine MV anterior and posterior leaflets and the region of interest for the 10mmx10mm MVAL specimen (C: circumferential direction and R: radial direction), and (b) experimental setup for the mini-biaxial testing, followed by histologic & thickness analyses (the first 7 μm section) and measurements of the MVIC NAR (the second 30 μm section) using MPM imaging.

Author Manuscript Author Manuscript Author Manuscript Author Manuscript

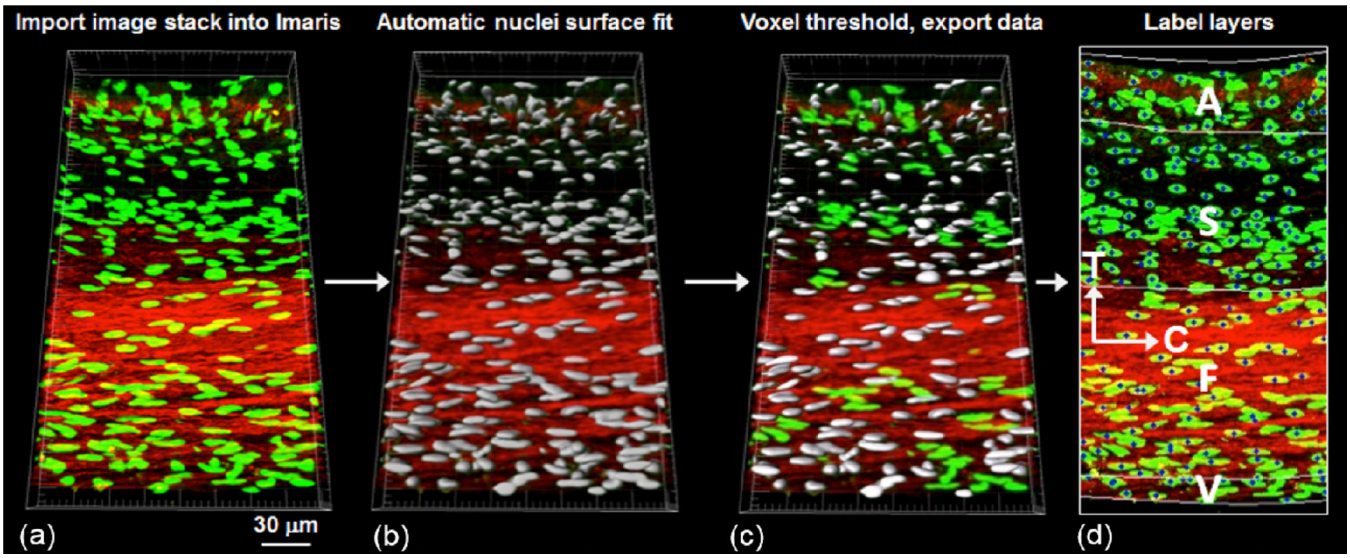

Figure 3.

Schematic of the MVIC deformation analysis procedure: (a) stack of images obtained from TPEF-MPM imported into Imaris for 3D visualization of Cytox Green stained MV interstitial cell nuclei, (b) automatic 3D surface fit to all cell nuclei using built-in analysis functions in Imaris, (c) exported voxel data with a specified threshold for gathering quantitative information, and (d) MV cell nuclei information associated with the four layers of the MVAL tissue using a MATLAB algorithm (C: circumferential direction, T: transmural direction).

Author Manuscript Author Manuscript Author Manuscript Author Manuscript

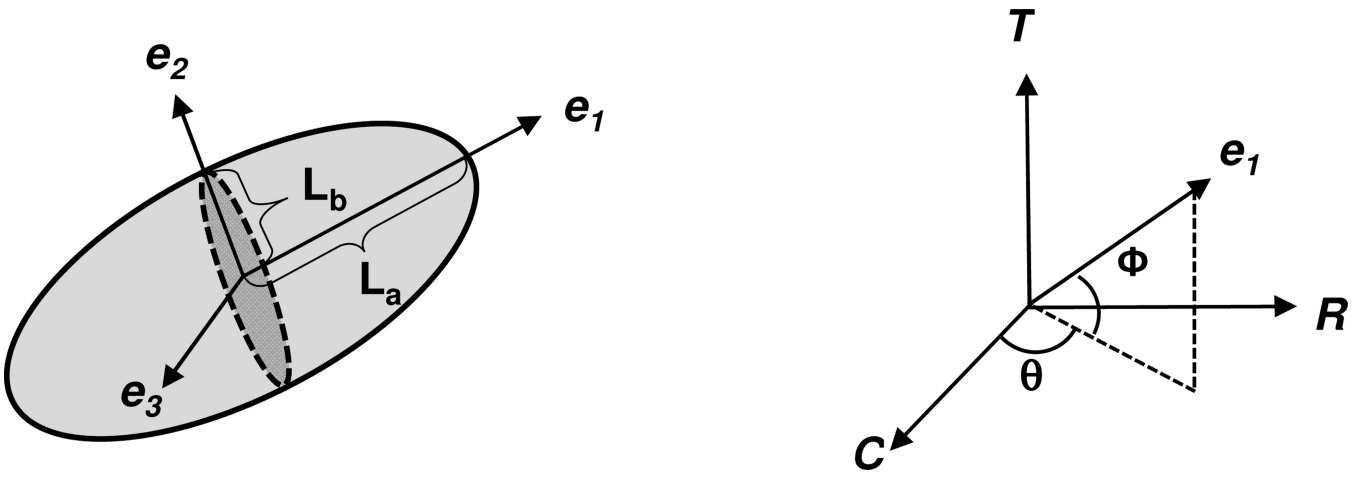

Figure 4.

(Left): schematic of the local coordinate system (e_1, e_2, e_3) defining the three principal axes of a MVIC nucleus based on the ellipsoidal geometry; (right): its orientation with respect to the global coordinate system (C: circumferential, R: radial direction, T: transmural direction).

Author Manuscript Author Manuscript Author Manuscript Author Manuscript

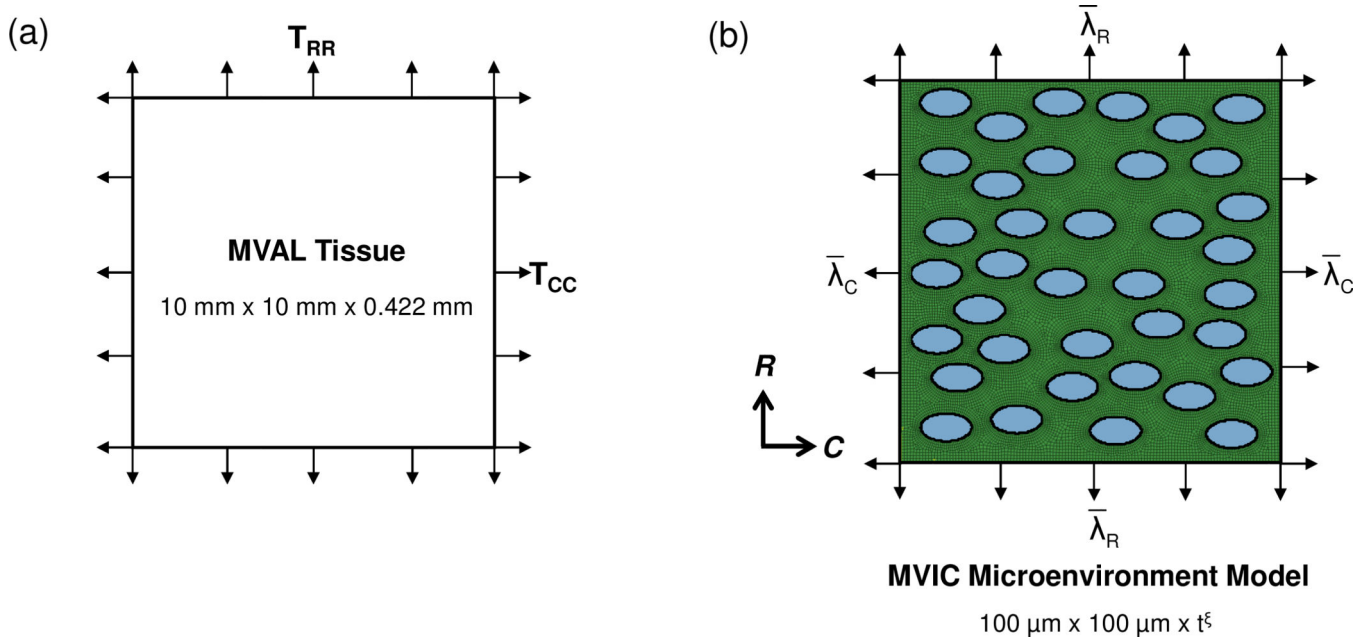

Figure 5.

The macro-micro finite element (FE) model utilized in our investigations of MVIC deformations: (a) schematic diagram of tissue-level modeling of the region of interest of the MVAL tissue under equi-biaxial tension loading, and (b) schematic diagram of MVIC microenvironment modeling with tissue-level deformations as prescribed boundary displacements considering 37 uniformly distributed MV interstitial cells embedded in the layer-specific representative volume element (RVE). (t^{ξ} denotes layer-specific thickness)

Author Manuscript Author Manuscript Author Manuscript Author Manuscript

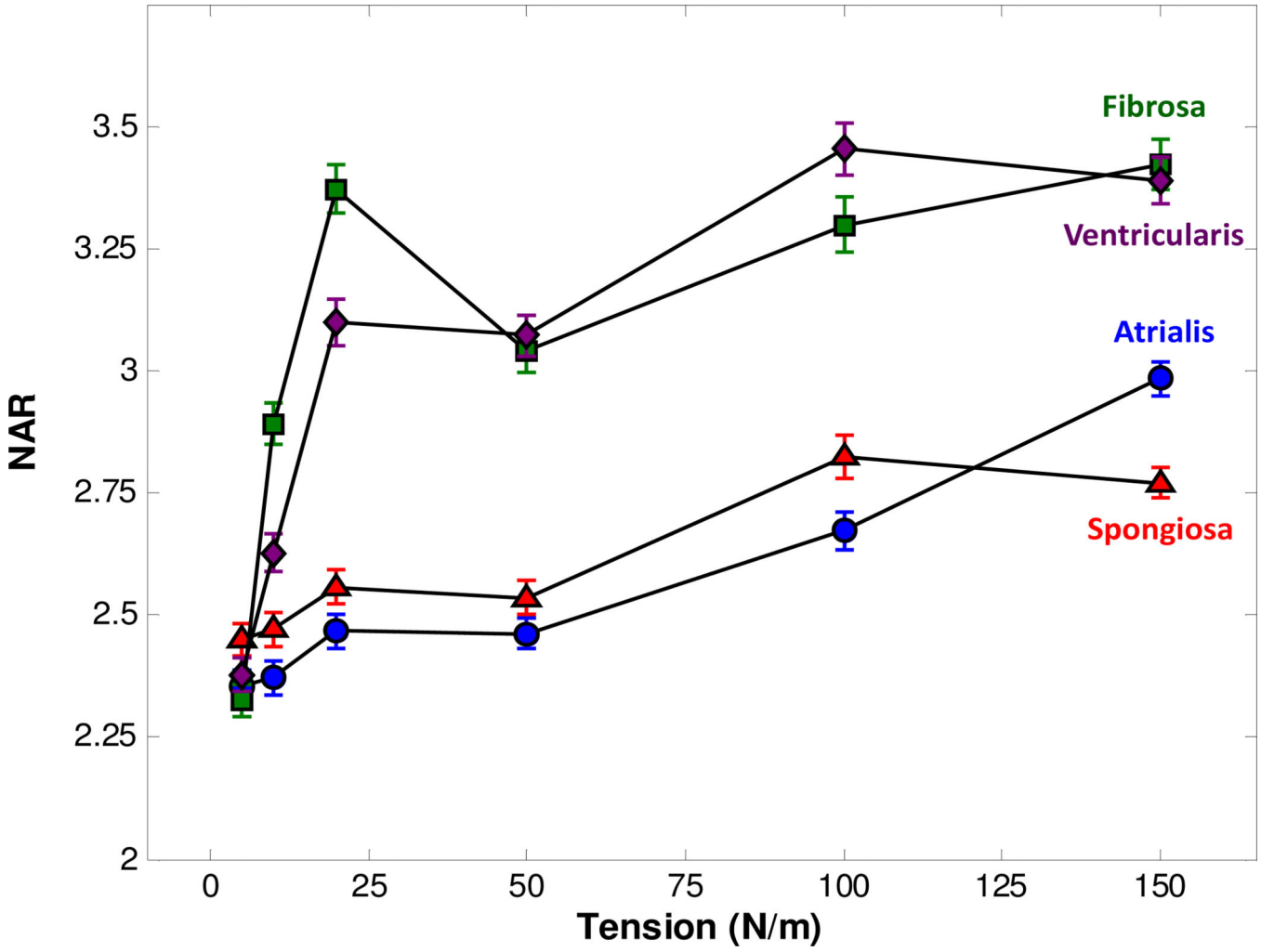

Figure 6.
MVAL layer-specific MVIC NAR as a function of applied biaxial tension, derived from MPM analysis.

Author Manuscript Author Manuscript Author Manuscript Author Manuscript

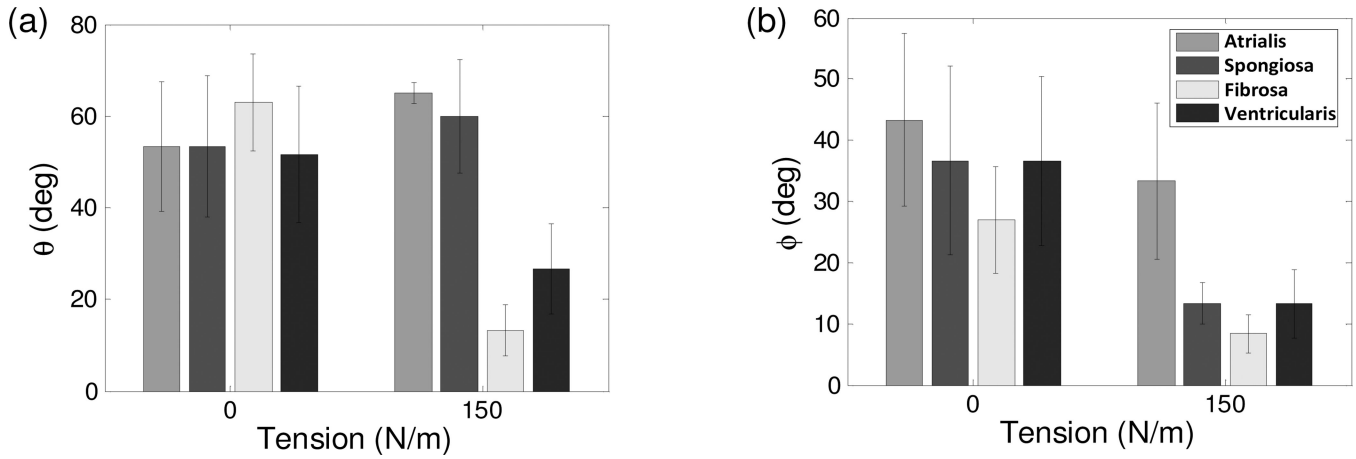

Figure 7.

(a,b) measured layer-specific orientation angles θ and φ at the unloaded configuration (0 N/m tension) and at the maximum loading state (150 N/m tension).

Author Manuscript Author Manuscript Author Manuscript Author Manuscript

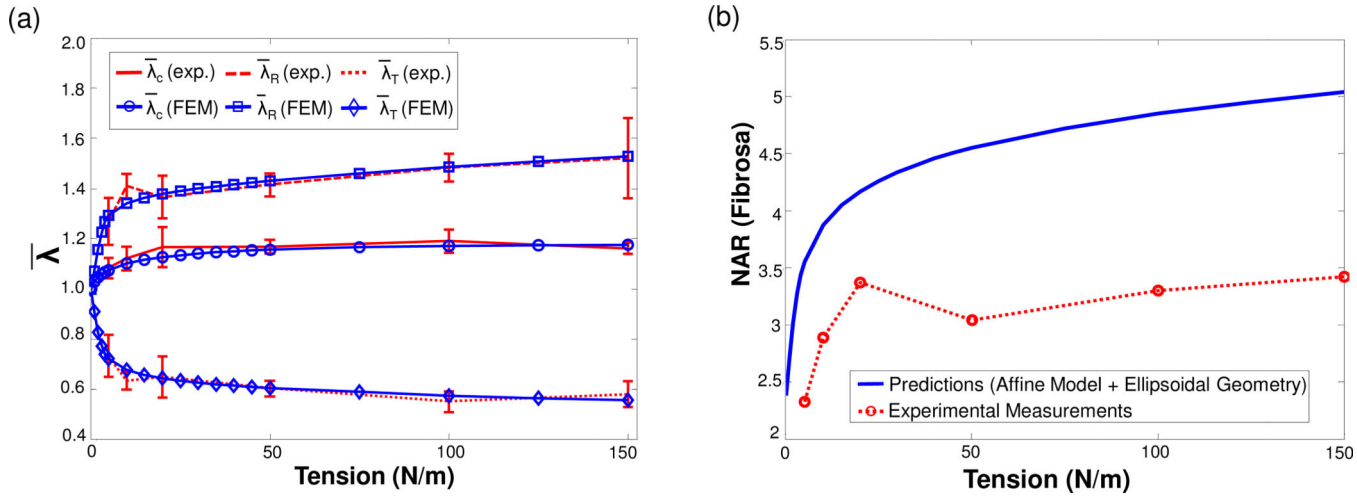

Figure 8.

(a) Comparison of the tissue-level deformations in terms of the three principal stretches between the experimental measurements and the FE predictions under equi-biaxial tension loading ($r^2 = 0.9896$), and (b) comparison of the fibrosa-layer MVIC NAR as a function of tissue-level tension between the experimental measurement and the calculation based on a simple affine model and an assumed ellipsoidal cellular geometry, indicating that local MVICs do not simply follow the deformation of the bulk MVAL tissue.

Author Manuscript Author Manuscript Author Manuscript Author Manuscript

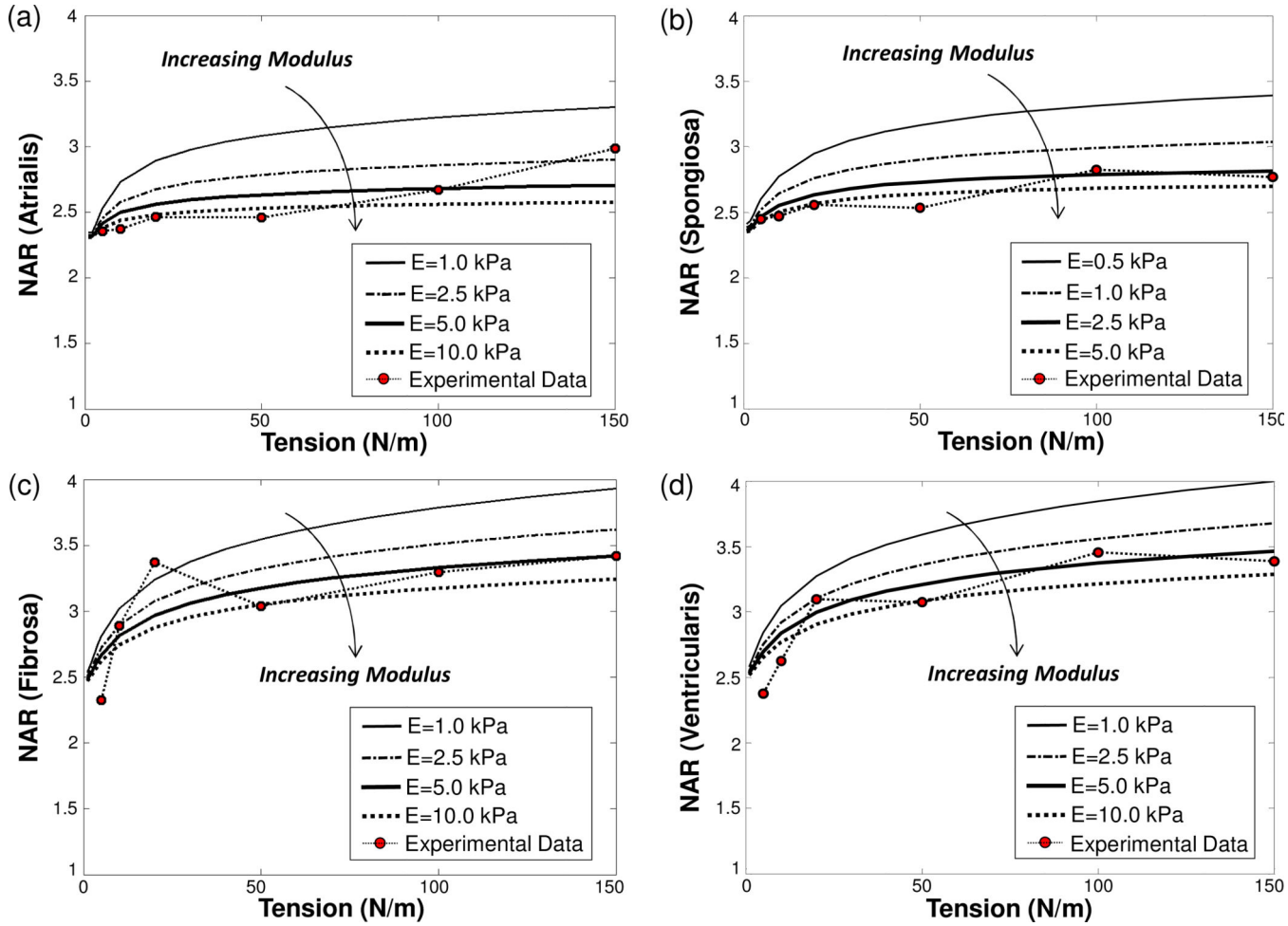

Figure 9.

Studies on the effect of the MVIC modulus on the predicted NARs: (a) atrialis layer, (b) spongiosa layer, (c) fibrosa layer, and (d) ventricularis layer.

Author Manuscript Author Manuscript Author Manuscript Author Manuscript

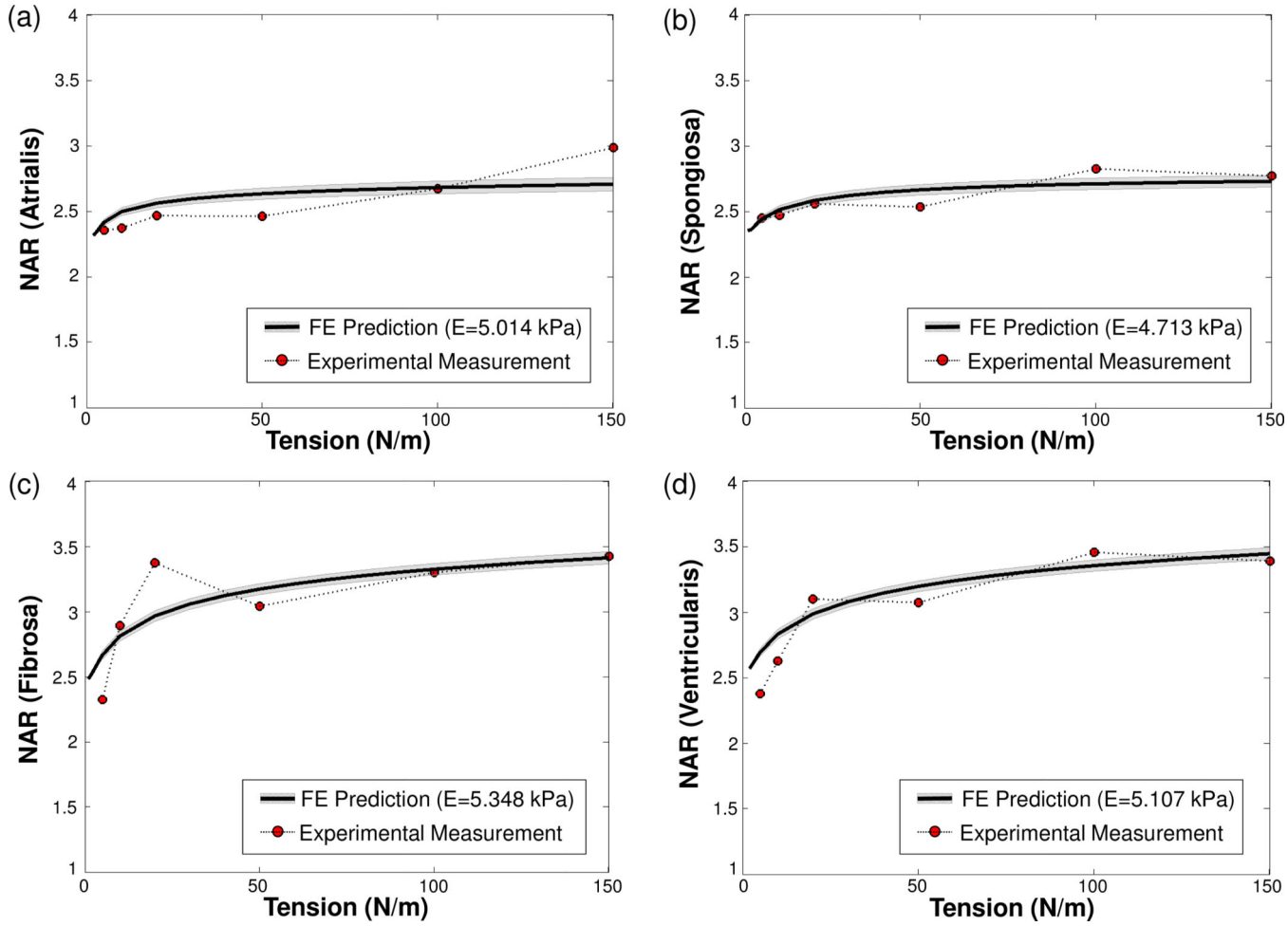

Figure 10.

Comparisons of the experimentally measured and numerically predicted NARs as a function of tissue-level tension (grey shaded area showing the standard deviation of the computed NARs over the 37 MVIC ellipsoidal inclusions): (a) atrialis layer (r^2 = 0.8403), (b) spongiosa layer (r^2 = 0.9166), (c) fibrosa layer (r^2 = 0.8906), and (d) ventricularis layer (r^2 = 0.9373).

Author Manuscript Author Manuscript Author Manuscript Author Manuscript

Table 1

MVAL Layer-specific structural and mechanical parameters

	MVAL Tissue Layers			
	Atrialis	**Spongiosa**	**Fibrosa**	**Ventricularis**
ECM Preferred Fiber Direction	**Radial**	**Radial**	**Circumferential**	**Circumferential**
Effective Fiber Orientation Index, OI^{ξ} (deg.)	21.86	81.97	30.25	30.25
Fiber Splay Standard Deviation, σ^{ξ} (deg.)	16.21	86.65	22.49	22.49
Thickness (μm)	43.2	41.5	319.6	17.3
MVIC Dimension in the Major Axis e_1, L_a (μm)	5.84	6.13	6.68	6.18
MVIC Dimension in the Minor Axis e_2, L_b (μm)	3.49	3.71	3.64	3.41
MVIC Nuclei Aspect Ratio at 0 N/m Tension, NAR_0	2.42	2.41	2.49	2.51
Collagen Mass Fraction, ω_c^{ξ}	0.231	0.203	0.671	0.309
Elastin Mass Fraction, ω_e^{ξ}	0.601	0.198	0.088	0.555
Matrix Mass Fraction, ω_m^{ξ}	0.168	0.599	0.241	0.136
Volume Fraction of Matrix, ϕ_m^{ξ}	0.017	0.059	0.182	0.006
Volume Fraction of Effective Fibers, $\phi_f^{\xi}=\phi_e^{\xi}+\phi_c^{\xi}$	0.085	0.039	0.576	0.036

Author Manuscript Author Manuscript Author Manuscript Author Manuscript

Table 2

Material parameters of the simplified structural constitutive model for the ovine MVAL tissue

	φ_m	φ_f	μ_m (kPa)	c_1 (kPa)	c_2	σ^a (deg.)
MVAL Tissue	0.264	0.736	28.41	0.917	22.13	36.85

[a]The standard deviation of the fiber angular orientation distribution function was the direct measurement from the small angle light scattering (SALS) test from the previous study of the excised ovine MVAL tissues (Lee et al., 2014).

J Theor Biol. Author manuscript; available in PMC 2016 May 21.

Author Manuscript Author Manuscript Author Manuscript Author Manuscript

Table 3

Comparisons of the MVIC NAR-tension responses in the fibrosa layer between the experimental data and numerical predictions with various considerations of the finite element model setup

Interstitial Cell Representation		**37 Uniformly Distributed MVICs**[a]		**Single MVIC with the Same Cell Volume Fraction**	**Experimental Measurements**
Material Model for MVIC Regions		**Saint-Venant Kirchhoff (E = 5.348 kPa)**	**Neo-Hookean (μ = 1.783 kPa)**	**Saint-Venant Kirchhoff (E = 5.348 kPa)**	
Tension (N/m)	5	2.661±0.031	4.299±0.088	2.718	2.325±0.0319
	10	2.804±0.038	4.671±0.101	2.831	2.891±0.0424
	20	2.999±0.041	5.038±0.103	2.963	3.372±0.0503
	50	3.156±0.042	5.579±0.105	3.146	3.039±0.0421
	75	3.243±0.043	5.863±0.109	3.227	–
	100	3.305±0.044	6.093±0.116	3.285	3.298±0.0568
	125	3.352±0.045	6.291±0.124	3.328	–
	150	3.391±0.046	6.469±0.132	3.363	3.422±0.0512

[a]The mean NAR and its standard deviation were obtained from the deformation states of the 37 populated cells.